Q. J. R. Meteorol. Soc. (1999), **125**, pp. 1129–1163

A mechanism relating tropical Atlantic spring sea surface temperature and west African rainfall

By XINYU ZHENG, ELFATIH A. B. ELTAHIR* and KERRY A. EMANUEL
Massachusetts Institute of Technology, USA

(Received 16 May 1997; revised 6 November 1998)

SUMMARY

In this paper, we describe a mechanistic study on the role of tropical Atlantic sea surface temperature (SST) variability in the dynamics of the west African monsoon. A hypothesis that a warm spring (April–June) SST results in a wet monsoon is explored using a moist, zonally symmetric model. A positive spring rainfall anomaly has been simulated over the ocean, in response to the warm SST, which then propagates onto the land and persists two to three months, even after the SST anomaly vanishes. While the ocean–atmosphere interaction is crucial for the initial development of the rainfall anomaly over land, the interactions between the ocean, land, and atmosphere are found to be important for relating tropical Atlantic spring SST to west African rainfall. Furthermore, the positive feedback between rainfall and soil moisture is responsible for some of the persistence in the rainfall anomaly. We present a case-study for the wettest (1994) and driest (1992) years of the 1990s so far. The observations show that a warm spring SST anomaly in 1994 was associated with abundant summer rainfall over west Africa. These empirical observations are consistent with the proposed physical mechanism.

KEYWORDS: Air–sea interaction Monsoons

1. INTRODUCTION

West Africa, especially the Sahel region, experienced a long episode of deficient rainfall from the late 1960s until recent years (see Nicholson and Palao 1993; Nicholson *et al.* 1996). Whether or not this trend will continue remains to be seen. Understanding the physical mechanisms responsible for the observed drought has motivated several studies.

Research studies on interannual variability of west African rainfall falls into one of two groups: efforts that investigate the response of the atmosphere to local land forcing and those that investigate teleconnections to the remote oceanic forcing (mainly the tropical Atlantic sea surface temperature (SST)). The land forcing includes changes of land surface boundary conditions, such as surface albedo and soil moisture level. Charney (1975) pioneered the study of land–atmosphere interaction in west Africa and presented a hypothesis for describing the mechanisms of droughts. His study, and subsequent ones (e.g. Charney *et al.* 1975, 1977; Cunnington and Rowntree 1986; Walker and Rowntree 1977; Xue and Shukla 1993; Zheng and Eltahir 1997; Zheng and Eltahir 1998a), conclude that local land surface forcing may play an important role in the dynamics of west African monsoon and rainfall.

The second group of studies is concerned with the role of the ocean, and in particular the global distribution of SST, in the regional climate of west Africa. The relationship between SST, especially the tropical Atlantic SST, and Sahel rainfall has been the focus of several studies. At the regional scale, Lamb (1978a) presented a case-study that shows that deficient sub-Saharan summer rainfall is associated with warm summer (July–September) SST anomalies and vice versa. He further studied the composite large-scale tropical Atlantic surface circulation patterns associated with sub-Saharan dry and wet years (Lamb 1978b). The dry composite shows negative SST anomalies during spring (April–June) and positive SST anomalies during summer. In contrast to this, the wet composite displays positive SST anomalies during spring and negative SST anomalies during summer (Fig. 5 and Fig. 6 in Lamb 1978b). A similar study by Lamb and Peppler (1992) confirmed the above results. Lough (1986) identified the dominant spatial patterns of normalized SST

* Corresponding author: Department of Civil and Environmental Engineering, Ralph M. Parsons Laboratory, Massachusetts Institute of Technology, Cambridge, Massachusetts 02139, USA.

departures in the tropical Atlantic Ocean using principal component analysis, and then correlated these different patterns with the rainfall anomaly in the Sahel region. There have been numerous studies of the correlation between Sahel rainfall and global SST anomalies (e.g. Glantz *et al.* 1991; Semazzi *et al.* 1988). All these statistical studies demonstrate that there is a strong association between west African rainfall and SST, both regionally and globally. However, most of these studies focus on the concurrent correlation between the summer rainfall and the summer SST and therefore do not elucidate any causal relations.

General circulation models (GCMs) have been used to investigate the impact of regional and global SST anomalies on west African rainfall variations (Folland *et al.* 1986; Druyan and Hastenrath 1991; Owen and Folland 1988; Palmer 1986; Palmer *et al.* 1992; Rowell *et al.* 1992, 1995). In particular, the study by Rowell *et al.* (1995) showed that their model was able to simulate the magnitude and pattern of the summer rainfall anomalies across tropical north Africa reasonably well. In addition, global SST variations were shown to be responsible for most of the summer rainfall variability. Although the results of Rowell *et al.* (1995) may be model-dependent and hence not conclusive (Sud and Lau 1996), they provide additional evidence for the connection between SST and rainfall. However, complex GCMs may not be the best tools for isolating detailed physical mechanisms linking SST and Sahel rainfall.

While most statistical and modelling studies discussed above are concerned with the concurrent correlation between summer SST and summer rainfall, there have been attempts to predict the sub-Saharan rainfall from SST anomalies several months in advance (e.g. Parker *et al.* 1988). Owen and Ward (1989) explored the possibility of forecasting the Sahel rainfall using spring SST observations by statistical methods. However, much remains to be understood about the physical links between spring SST and Sahel rainfall.

In general, both local land surface forcing and remote SST forcing may be responsible for the observed variability in Sahel rainfall. Besides these boundary forcings, internal atmospheric variability may also play some role. Our major aim here is to elucidate the important physical processes that relate regional SST anomalies and African rainfall variability. We hypothesize that spring SST anomalies in the tropical Atlantic Ocean affect summer rainfall in west Africa. We then use a zonally symmetric numerical model as a regional model of west African monsoons to explore this hypothesis. Since the model is two-dimensional, it does not include zonally asymmetric disturbances (e.g. synoptic disturbances) which are responsible for some internal atmospheric variability. However, as pointed out by Rowell *et al.* (1995) regarding the seasonal rainfall variability, the internal variability is secondary compared to boundary layer forcing such as SST variability. The simple dynamical framework of our model allows us to perform detailed process studies. We conclude by presenting a case-study comparing the dry year of 1992 and the wet year of 1994, interpreting the observations for these two years in the light of the proposed hypothesis.

2. Numerical experiments

In what follows, we use a numerical model to address the possible impact of SST on west African rainfall. While our model is designed as a process model, it does capture the essential features of the observed west African monsoon (e.g. rainfall and wind patterns). Because of its simplicity, the model is expected to deviate from the observations to some extent, for example in the magnitude of the variability. However, we expect this model to capture the main patterns of the ocean–land–atmosphere interactions revealed by the observations. The advantage of this model is that it allows us to explore the mechanisms

in great detail. The results in this paper will guide our future research, within the context of a more realistic model.

(a) *Model description*

Observations indicate that the distributions of vegetation, temperature, specific humidity and rainfall in west Africa are approximately uniform in the zonal direction. More importantly, the quantitative analysis presented by Zheng and Eltahir (1998a; ZE98 hereafter) shows that the effect of zonal asymmetries is of secondary importance in west Africa. Therefore, it seems reasonable to adopt a zonally symmetric dynamical framework in this region. The model we employ is designed as a process model and is not meant to simulate the details of the variability of the natural system. Instead, a limited set of essential processes is included in order to investigate the dominant physical processes that may be important for simulating realistic monsoons. Our purpose here is to use this relatively simple model to identify some potentially important mechanisms, which should then be tested using more complicated models (e.g. GCMs) and against observations.

The model used here is very similar to that described by ZE98, with some important modifications. The model domain is global horizontally and extends from the surface up to 25 km in log-pressure coordinates. The grid points are evenly spaced in sine latitude with 46 increments (about 2.5° resolution in terms of latitude in the tropics), and also equally spaced vertically with 25 increments (1 km vertical resolution). The model is hydrostatic and uses primitive momentum equations. An explicit hydrological cycle is incorporated. The model uses a fast radiation parametrization scheme developed by Chou *et al.* (1991) and the interaction between clouds and radiation is neglected. The ensemble effect of moist convection (both deep and shallow) is parametrized using the Emanuel scheme (Emanuel 1991). For a detailed description of the model physical processes, refer to ZE98.

The model domain represents a longitudinally averaged latitude–height cross-section. Therefore, our model results should be compared with the longitudinally averaged observations from 15°W to 15°E. The surface is considered to be land north of 5°N (which is assumed to be the location of the southern Atlantic coast) and ocean south of 5°N. The control experiment uses the SST climatology from 1981 to 1995. The SST data used here are taken from the monthly optimal interpolation (OI) SST analysis, which uses in situ observations and satellite-derived SSTs (Reynolds and Smith 1994). Since the dataset only provides monthly averaged values, we apply linear interpolation within the time domain. We assume that the monthly SST represents the SST at the mid-month day (e.g. January SST is set equal to the SST on 15 January). The SST at any time between two consecutive mid-month days (e.g. 15 April to 15 May) is based on linear interpolation. Since our model is zonally symmetric, we have to ignore zonal variations of SST. Nevertheless, the typical SST pattern in the southern tropical Atlantic Ocean shows that the meridional gradient is larger than the zonal gradient (not shown here). We use the longitudinally averaged values from 5°W to 5°E as model input.

The major difference between this model and the model used in ZE98 is the treatment of the land surface processes. The land surface temperature was assumed to be determined by the surface energy balance in ZE98. In other words, the land had zero heat capacity. This assumption was justified by the fact that the land heat capacity is much smaller than that of the ocean. In fact, this assumption does not influence the results in ZE98 since only steady-state solutions were considered there. Here we are concerned with the seasonal migration of west African rainfall; we therefore assume a finite land heat capacity. This modification is not essential, but the inclusion of the finite land heat capacity does have an impact on multi-day time scales as we will show later. We follow Srinivasan *et al.* (1993)

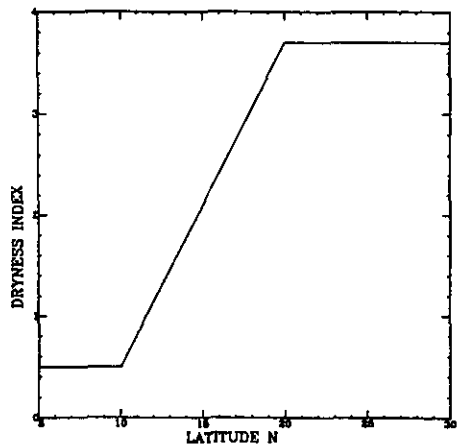

Figure 1. The latitudinal distribution of the dryness index for the control experiment.

and use the effective soil volumetric heat capacity per unit area $C_E = 4.5 \times 10^6$ J m^{-2}K^{-1}. The land surface temperature equation is:

$$C_E \frac{\partial T_g}{\partial t} = R_{net} - SH - L_v E, \tag{1}$$

where T_g is the ground temperature; t is time; R_{net} is the surface net radiative flux (positive downward); SH is the surface sensible-heat flux; $L_v E$ is the surface latent-heat flux, with L_v the latent heat of vaporization and E the surface evaporation.

Following ZE98, we also use the Budyko (1974) climate index of dryness as an indicator of the vegetation type. The vegetation type basically determines the depth of the root zone and therefore the field capacity. We assume a latitudinal profile of the dryness index of west Africa (see Fig. 1) which is similar but not identical to ZE98. This profile is meant to mimic qualitatively the distribution of the actual natural vegetation in west Africa. In general, the dryness index has a small value (less than 1) within the tropical forest region and increases northward, achieving a maximum (greater than 3) in the desert region. This dryness index pattern roughly depicts the distribution of the vegetation type in west Africa, from tropical forest near the southern Atlantic coast to the semi-arid plants (grasslands, shrubs) in the Sahel and the Sahara desert. The analytical form of the assumed dryness index is:

$$D = \begin{cases} 0.5 & \phi_0 \leqslant \phi \leqslant \phi_1 \\ 3.7 + (3.7 - 0.5)\dfrac{\phi - \phi_2}{\phi_2 - \phi_1} & \phi_1 \leqslant \phi \leqslant \phi_2 \\ 3.7 & \phi > \phi_2, \end{cases} \tag{2}$$

where ϕ is latitude; $\phi_0 = 5°$N (coast line); $\phi_1 = 19°$N; and $\phi_2 = 20°$N.

We follow Gutman *et al.* (1984) and relate the field capacity (W_c) to the dryness index (D)

$$W_c = W_0 \frac{\tanh D}{D}, \tag{3}$$

where $W_0 = 80$ cm (Dickinson *et al.* 1986). This simply means that the maximum soil

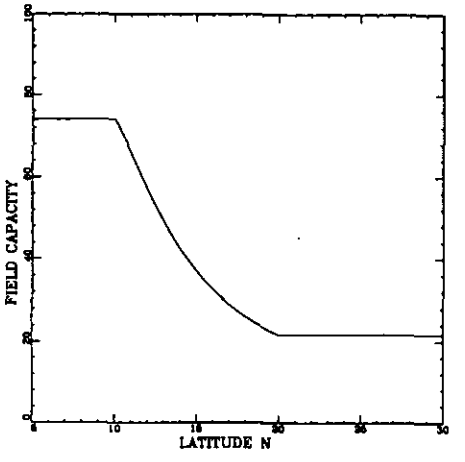

Figure 2. The latitudinal distribution of the field capacity in centimetres for the control experiment.

moisture depends on the vegetation type (depth of the root zone), as indicated by the dryness index here. The latitudinal profile of the field capacity is shown in Fig. 2.

As a simple soil hydrology scheme, we use the bucket model (Manabe 1969). What is different is that in Manabe (1969) the field capacity was held constant, but here our field capacity has a latitudinal variation. The soil moisture prognostic equation is:

$$\frac{\partial W}{\partial t} = \begin{cases} 0 & W \geqslant W_c \text{ and } P \geqslant E \\ P - E & \text{otherwise} \end{cases} \tag{4}$$

where P is precipitation. Any excessive soil moisture above field capacity is considered to be run-off. The evaporation is evaluated according to the relative saturation of the soil moisture ($\frac{W}{W_c}$) and potential evaporation E_p which is parametrized by a bulk formula (exchange coefficients are 1.0×10^{-3} over ocean and 2.0×10^{-3} over land):

$$E = E_p \left(\frac{W}{W_c}\right)^{\beta}; \tag{5}$$

β is generally taken as 1.0.

The Earth Radiation Budget Experiment observations indicate that the surface albedo (α) of west Africa has quite a zonally uniform distribution (Darnell *et al.* 1995), supporting our adoption of the zonally symmetric framework. In addition, the surface albedo was found to be high (as high as 48%) over the Sahara desert. Here we assume an analytical form of albedo versus dryness index to mimic the observed albedo pattern, shown in Fig. 3:

$$\alpha = \begin{cases} \min(0.48,\ 0.014 + 0.126D) & D \geqslant 1 \\ 0.14 & 0 < D < 1. \end{cases} \tag{6}$$

Note that within the tropical forest region, there is no dependence of the surface albedo on the dryness index (Gutman *et al.* 1984). We take into account the effect of soil moisture on the surface albedo by multiplying the surface albedo defined in (6) by a factor $(1 - 0.5\frac{W_s}{W_c})$ for all regions except tropical forest regions (defined as the region where $D \leqslant 1$) where the albedo is held as 0.14. This means that the saturation of the soil can decrease the albedo defined in (6) by 50% for fully saturated soil. The oceanic surface albedo is taken as 0.06.

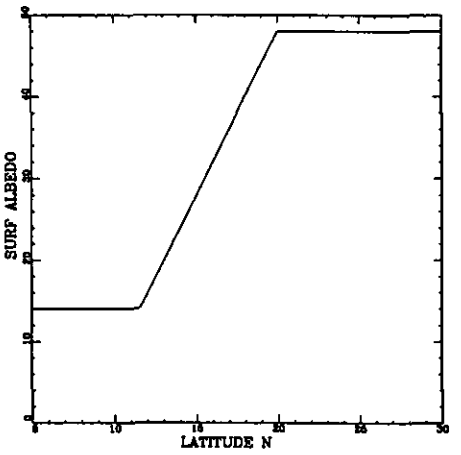

Figure 3. The latitudinal distribution of the surface albedo as percentages for the control experiment.

(*b*) *Control run*

The control run is forced by the observed 1981–1995 climatological SST. The solar forcing has a seasonal cycle (no diurnal cycle). The model is first integrated for 300 days by fixing the solar insolation at the spring equinox. This produces the initial state for subsequent runs with seasonally varying solar insolation. This model is integrated over a long enough period (about two to three years) to get a statistically equilibrated annual cycle, which is used as our control atmosphere. A multi-year model integration shows that the equilibrated annual cycle has very little interannual variance.

The total rainfall of the control experiment shows the migration of a rainband from over the ocean in winter onto the land in summer (Fig. 4). Compared with observations (see Fig. 5), the model successfully simulates the gross features of the seasonal cycle of the west African rainfall. The rainfall dataset we use here is that of the Global Precipitation Climatology Project (GPCP; Huffman *et al.* 1995). For example, the intertropical convergence zone (ITCZ; location of the maximum rainfall) achieves its northernmost position in August, as observed (Fig. 5). In addition, the latitude of this position is roughly the same as that of the observations (10–12°N). Also, both the observations and model latitudinal distributions of the total rainfall in August (Fig. 6) show a sharp gradient of rainfall from the position of the ITCZ (~12°N) northward to the desert (20°N). The comparison of the latitudinal profiles of rainfall between the model and the observations indicates a generally good agreement in terms of the location of the ITCZ and the north–south gradient of the rainfall. In addition, the seasonal cycle of the rainfall over the Sahel region (from 10°N to 20°N) displays similarity to the observations, although the model overestimates the rainfall magnitude, as can be seen in Fig. 7. This may have to do with the neglect of zonal asymmetries. As demonstrated in ZE98, the zonal asymmetries result in a net moisture divergence out of the west African region. In other words, the zonally symmetric models tend to exaggerate moisture convergence into the region (others factors being the same).

On the other hand, the winter rainfall (December–February) over the ocean is much heavier than in the observations. This also has to do with the assumption of zonal symmetry. One reason for this may be that the model lacks meridional heat transport due to zonally asymmetric eddies (dominant in winter), and the surface temperature gradient between

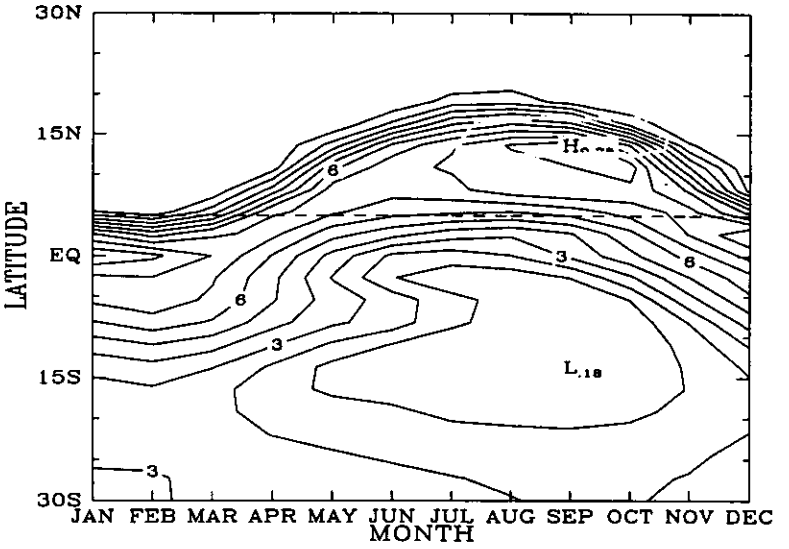

Figure 4. The latitude–time total rainfall distribution from the control experiment; the contour interval is 1 mm day^{-1}.

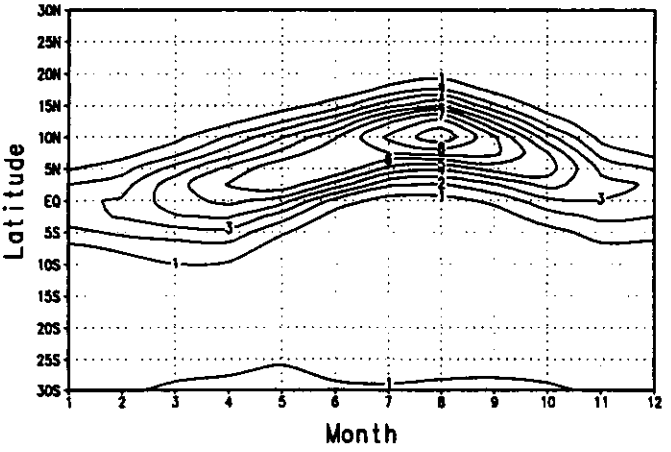

Figure 5. The latitude–time GPCP (see text) rainfall climatology from 1988 to 1994, averaged from 15°W to 15°E, the contour interval is 1 mm day^{-1}. Note that since data for December 1994 are missing, the December climatology comprises averages from 1988 to 1993.

the warm ocean and the cold land is unrealistically large, producing a strong updraught over the warm ocean. Secondly, the observed maximum winter rainfall actually occurs in the southern African land region instead of over the Atlantic Ocean. This would produce subsidence elsewhere and hence unfavourable conditions for the development of rainfall over the Atlantic Ocean. Obviously, this mechanism is missing in our two-dimensional model.

The soil moisture shows a smooth seasonal cycle (Fig. 8). In combination with the seasonal cycle of large-scale moisture convergence (Fig. 9), we see that the soil moisture

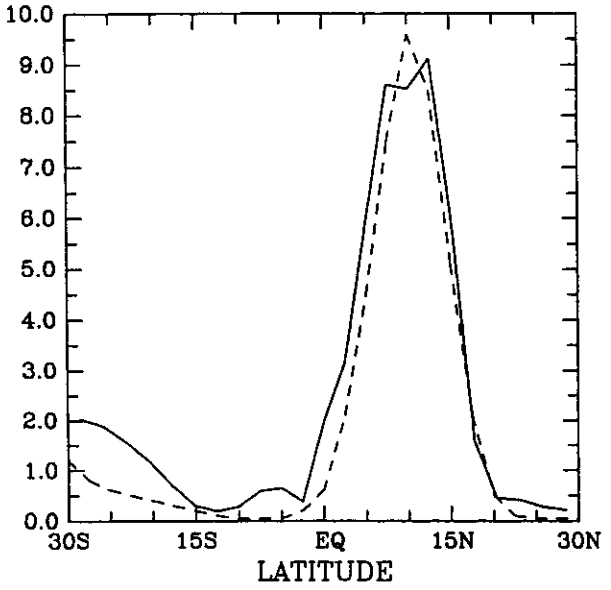

Figure 6. The latitudinal profile of the total rainfall in August for the control experiment (solid line) and the observed 1987 to 1994 GPCP (see text) August climatology (dashed line), averaged from 15°W to 15°E.

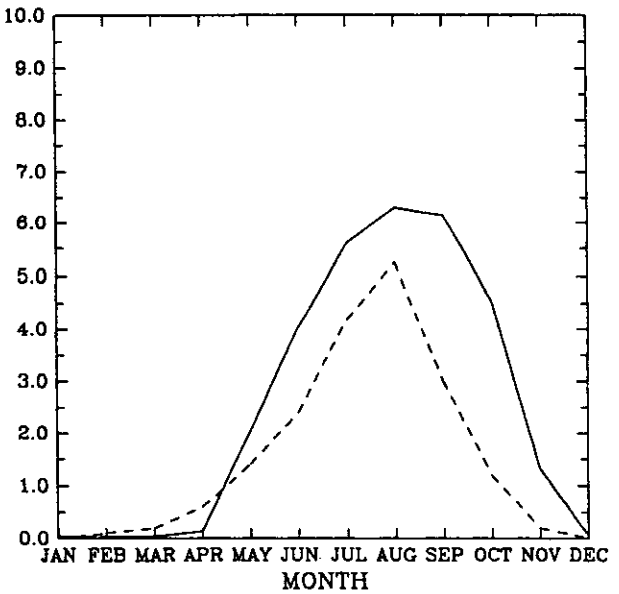

Figure 7. The time series of the total rainfall over the region from 10°N to 20°N for the control run (solid line) and the observed 1988 to 1994 GPCP (see text) rainfall climatology (dashed line).

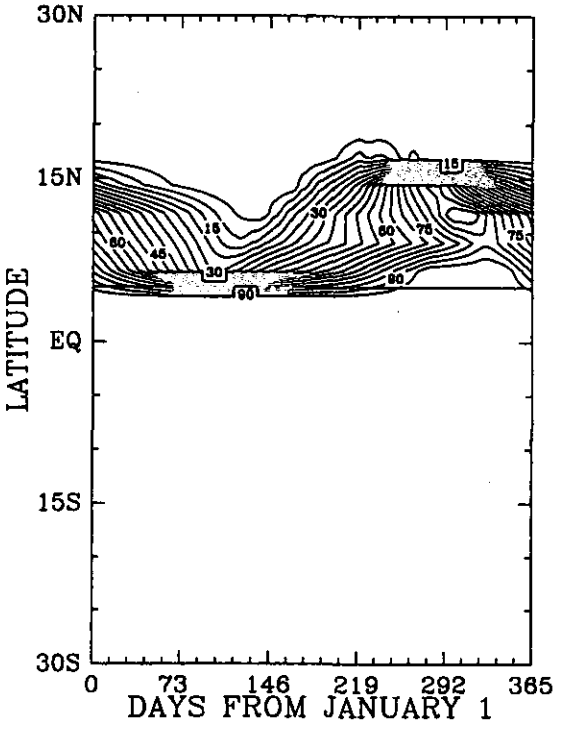

Figure 8. The relative soil moisture (ratio between soil moisture and field capacity) latitude–time cross-section for the control case; the contour interval is 5.

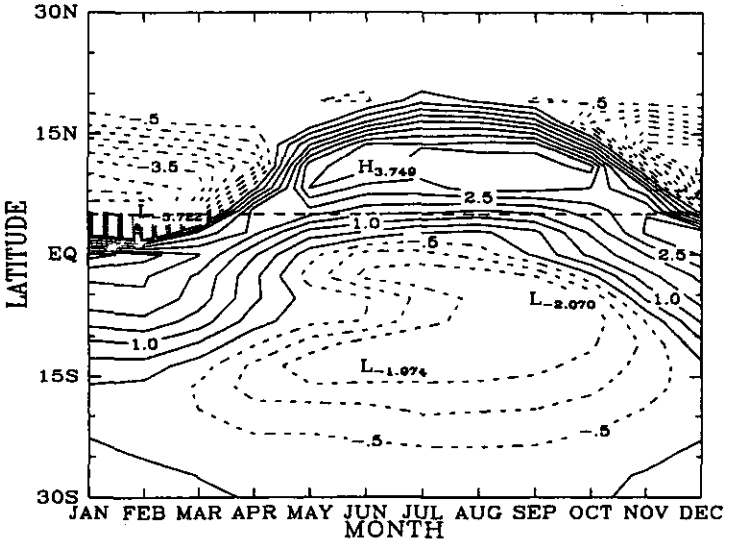

Figure 9. The large-scale convergence expressed as the difference between total rainfall (P) and local evaporation (E) for the control experiment; the contour interval is 0.5 mm day^{-1}.

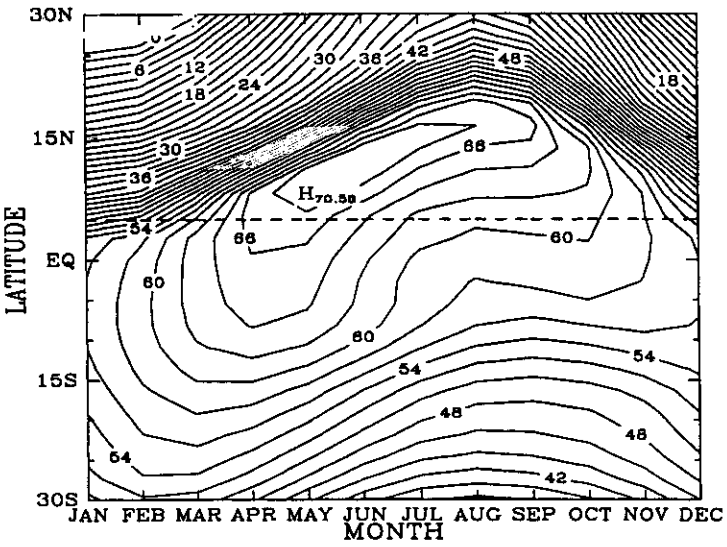

Figure 10. The boundary layer equivalent potential temperature θ_e (°C) for the control experiment; the contour interval is 2 degC.

follows the pattern of the large-scale moisture convergence, as indicated by (4). Because the large-scale moisture convergence is negative over the land in winter, the soil moisture decreases and achieves its minimum in spring. Likewise, the rainfall maximum occurs in August and September and the maximum soil moisture occurs in late October.

We emphasize that the boundary layer entropy is the key variable in the dynamics of moist atmospheres (Emanuel 1995; Eltahir and Gong 1996). The model surface air moist entropy expressed in terms of equivalent potential temperature, θ_e, is shown in Fig. 10. The distribution of boundary layer θ_e by no means resembles the details of the observations (not shown here). For example, the observed maxima of θ_e in September and October at latitudes near 12°N are not well simulated. But if we look at the line of maximum θ_e, we do see in the model a maximum in September and October. The difference is largely due to an unrealistic model winter simulation, which is probably attributable to the lack of northward heat transport by eddies. The model surface air temperature and specific humidity (not shown here) also show patterns similar to those of observations. The major caveat of the control experiment is the unrealistic winter scenario, as we mentioned earlier.

Although the overall pattern of the surface air θ_e bears a resemblance to the observations, our model control experiment does deviate substantially from the observations quantitatively. This implies that our model sensitivity to surface anomalies might differ from that of the European Centre for Medium-Range Weather Forecasting (ECMWF) data. In other words, for the same surface anomaly (such as an SST anomaly), the model may have a different response from the real world, especially in terms of the rainfall magnitude (recall that our model does a much better job at rainfall simulation.) However, since the model is able to capture the essential rainfall spatial and temporal patterns over west Africa, it allows us to investigate the physical mechanisms that might be relevant to real west African rainfall variability. In order to obtain significant model anomaly patterns, we specify a larger-than-observed magnitude of SST anomalies. We do not expect the model to be able to simulate the exact variability (e.g. anomaly magnitude) of the real atmosphere, but we do expect the model to simulate the correct anomaly patterns.

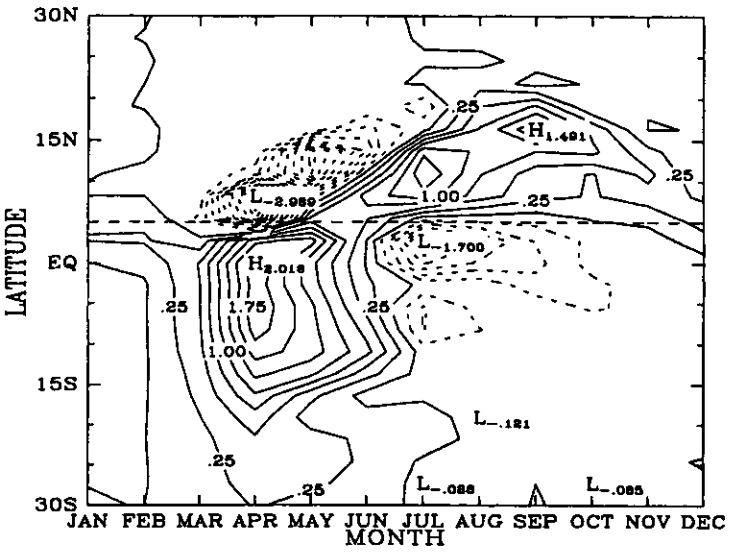

Figure 11. The total rainfall anomaly caused by the specified SST anomaly (magnitude of $T_{max} = 3.0$ K) for April–June; the contour interval is 0.25 mm day^{-1}.

(c) *Hypothetical anomaly experiments*

Here we apply hypothetical SST anomalies (superimposed on the monthly SST of the 1981–1995 climatology) to the control experiment. We specify the anomaly as a Gaussian distribution:

$$T' = T_{max}\, e^{-\left(\frac{\phi-\phi_c}{\delta\phi}\right)^2}, \tag{7}$$

where T' is the monthly SST anomaly; ϕ is the latitude; ϕ_c is the latitude of the maximum T' and $\delta\phi$ is the half-width in latitude. We take $T_{max} = 3.0$ degC, $\phi_c = 10°$S, and $\delta\phi = 30°$. The assumed SST anomaly pattern loosely mimics that revealed by Lough (1986). Note that the SST anomaly is interpreted as the value at the mid-month day (e.g. the January SST anomaly is set at January 15), just as in the control experiment. The SST anomaly between any two mid-month days is calculated by linear interpolation.

We divide the year into four quarters: January to March, April to June, July to September, and October to December. We first discuss a set of four SST anomaly experiments. These four experiments include imposing the SST anomaly given by (7) in January–March, April–June, July–September, and October–December, respectively. This set of experiments is designed to explore the role of the timing of SST anomalies. For each experiment, the model is integrated over a long enough period (about two years) to get a statistically equilibrated annual cycle. This is compared with the control experiment. We find that SST anomalies imposed in winter months (October–March) have the least influence on the summer rainfall (not shown here). On the other hand, spring SST anomalies induce substantial summer rainfall anomalies (Fig. 11). (In section 4, we compare the rainfall anomaly pattern caused by the spring SST anomaly with the pattern of the observed rainfall difference between 1994 and 1992.) A positive rainfall anomaly emerges over the ocean in spring in response to the warm SST anomaly; at the same time, a negative rainfall anomaly appears over the land. The positive rainfall anomaly appears to propagate onto the land as summer arrives. This experiment will hereafter be referred to as the standard spring SST

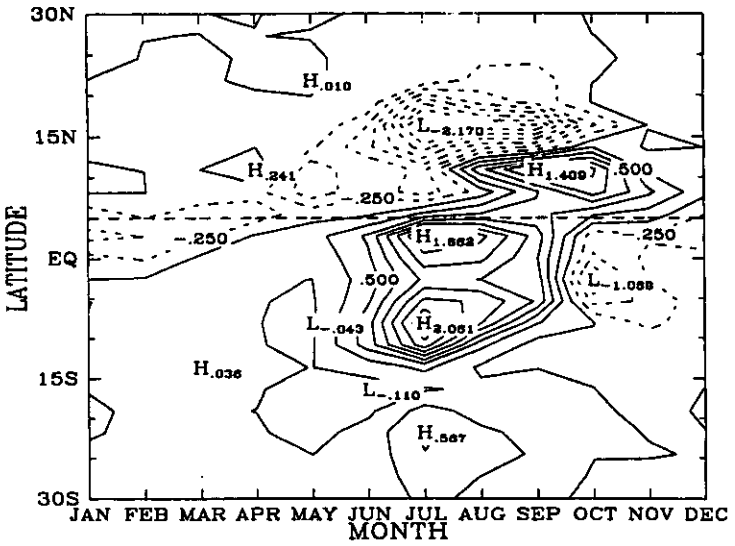

Figure 12. The total rainfall anomaly caused by the specified SST anomaly (magnitude of $T_{max} = 3.0$ K) for July–September; the contour interval is 0.25 mm day^{-1}.

anomaly experiment. Finally, the summer SST anomaly causes a negative summer rainfall anomaly over the land, consistent with previous studies (e.g. Lamb 1978a,b), but we do see a similar positive rainfall anomaly propagation from the ocean onto the land (Fig. 12). As a result, the rainfall in late summer and early autumn has a positive anomaly over the land although the anomaly is confined to south of 10°N.

The above experiments suggest that Atlantic spring SST anomalies are positively correlated with the west African summer rainfall, whereas summer SST anomalies are negatively correlated with the summer rainfall. Therefore, a positive spring SST anomaly plus a negative summer SST anomaly is favourable for abundant summer rainfall in west Africa. This finding is qualitatively consistent with the composite study of Lamb (1978b, Figs. 5 and 6). The winter SST anomalies in general have relatively minor impact on the summer rainfall. In what follows, we will look into the mechanisms behind these results. In particular, our main focus will be on the mechanisms of the rainfall anomaly pattern caused by the spring SST anomaly.

3. Mechanisms

(*a*) *Other details of the standard spring SST anomaly experiment*

We have seen from Fig. 11 that the spring SST anomaly first produces a positive rainfall anomaly over the ocean and a negative rainfall anomaly over the land. Since the dynamics of the thermally direct circulation in moist atmospheres is regulated by the gradient of the boundary layer entropy (ZE98), the warm SST anomaly decreases the land–ocean contrast and therefore causes less rainfall over the land in spring. What is interesting in this experiment is the apparent positive rainfall anomaly propagation onto the land. In addition, we see that the rainfall anomaly persists about two to three months after the SST anomaly vanishes, and in fact reaches its maximum value in September.

The rainfall anomaly pattern caused by the spring SST anomaly is mainly associated with the change of circulation, as can be seen from the anomaly pattern of large-scale

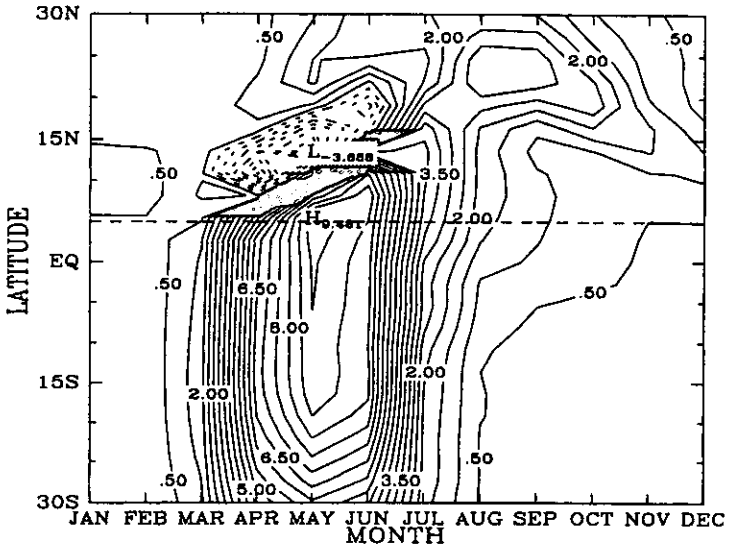

Figure 13. The boundary layer entropy anomaly (K) caused by the specified SST anomaly (magnitude of T_{max} = 3.0 K) for April–June; the contour interval is 0.5 K.

moisture convergence (not shown here). Following the anomaly pattern of the moisture convergence, the soil gets drier over the land during spring and early summer and then gets wetter as the rainfall arrives later on (not shown). The relatively wet soil in late summer produces more evaporation (not shown) and therefore a cooler land surface (not shown). The boundary layer entropy anomaly (expressed by θ_e) is basically consistent with the rainfall anomaly pattern, confirming the notion that the gradient of entropy dictates the intensity of monsoon circulations (Fig. 13). Next we examine in more detail the role of individual processes in the development of the rainfall anomaly pattern shown in Fig. 11.

(*b*) *Role of soil moisture*

Soil moisture in our model responds to precipitation and has an effect on both surface albedo and evaporation. In general, wet soil-moisture conditions result in smaller surface albedo and larger surface evaporation. These conditions enhance net surface radiation (Eltahir 1998). The increase of net surface radiation then causes an increase in the total heat flux from the surface, and therefore in the boundary layer entropy. The increase of boundary layer entropy has two effects. At local scales, the increase of boundary layer entropy would tend to destabilize the atmosphere and favours more rainfall. At larger spatial scales, the increase of boundary layer entropy is also likely to strengthen the large-scale monsoon circulation by enhancing the gradient of boundary layer entropy. Therefore, the soil moisture–rainfall feedback is likely to be positive. However, this feedback is not just a pure recycling of water through increased evaporation; it involves radiative and dynamical processes. The detailed analysis of the soil moisture–rainfall feedback mechanism can be found in Zheng and Eltahir (1998b). Here we describe an anomaly experiment with exactly the same SST anomaly as the standard spring SST anomaly experiment, but with soil moisture fixed at the values of the control experiment. The resulting rainfall anomaly is shown in Fig. 14. Apparently, the rainfall anomaly does not last as long as that of the standard spring SST anomaly experiment (Fig. 11). For example,

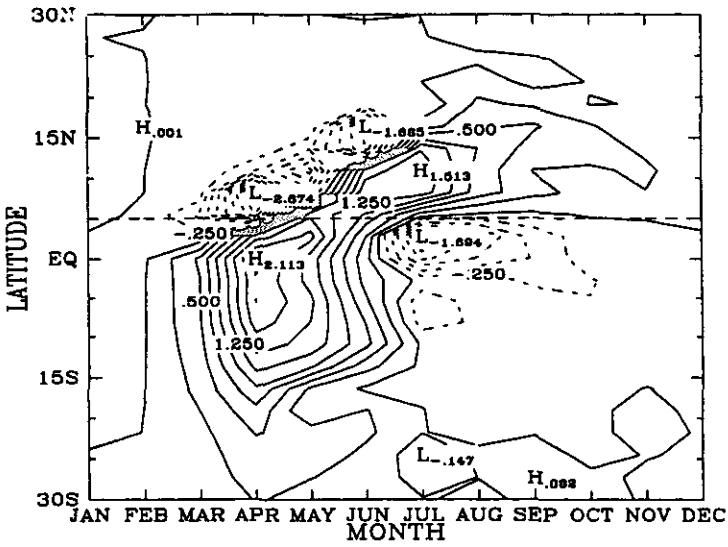

Figure 14. The total rainfall anomaly caused by the specified SST anomaly (magnitude of $T_{max} = 3.0$ K) for April–June. The soil moisture is fixed at the same values as in the control experiment. The contour interval is 0.25 mm day^{-1}.

the rainfall anomaly maximum in September observed in the standard spring SST anomaly experiment disappears. By fixing the soil moisture the rainfall anomaly vanishes before September, whereas in the standard anomaly experiment the rainfall anomaly lasts until November. It is clear that the soil moisture–rainfall feedback sustains the initial rainfall anomaly two to three months longer than otherwise. On the other hand, the rainfall anomaly migration pattern still exists. That is, the initial positive rainfall anomaly propagates onto the land after about one to two months.

The time-scale over which the soil moisture anomaly is sustained can be estimated as follows. Following (4), the soil moisture equation can be written approximately as:

$$\frac{\partial W}{\partial t} = P - \frac{E_p}{W_c} W.$$

From this, we see that the decay time-scale of soil moisture can be approximated as $\frac{W_c}{E_p}$ (P is the forcing mechanism). This time-scale can be interpreted as the lower bound of the time-scale over which the soil moisture anomaly is sustained, because this is the time-scale when P is considered as an independent forcing of W (see Delworth and Manabe, 1988). Figure 15 shows the time-scale estimated from this method. Although the damping time-scale of soil moisture has large spatial and temporal variabilities, it ranges from one to two months for the region where the soil moisture–rainfall feedback is dominant (comparing Fig. 11 and Fig. 14). This time-scale is smaller than that over which the rainfall anomalies are actually sustained (about 3 months), consistent with the notion that this is a lower bound. Notice that for the desert region (north of 20°N), the soil moisture damping time-scale is a lot shorter because of much greater potential evaporation there.

The experiment we described in this section suggests that interactive soil moisture is essential for sustaining the rainfall anomaly. Without the feedback between rainfall and soil moisture, the rainfall anomaly caused by the imposed spring SST anomaly cannot sustain

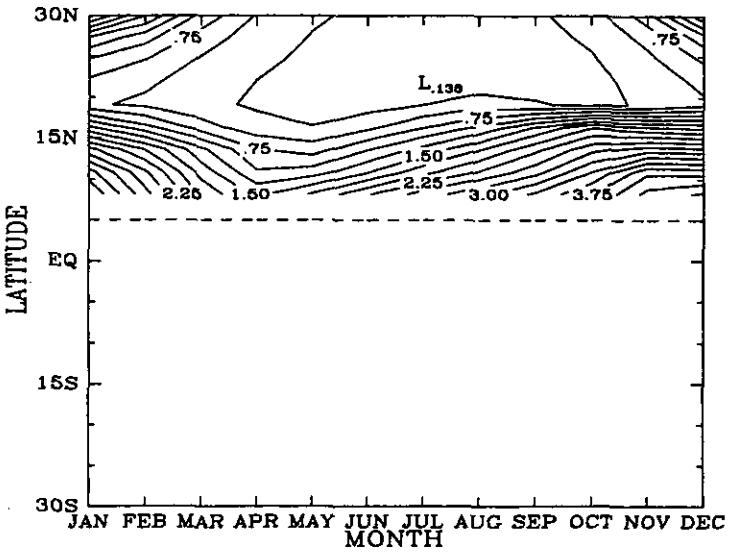

Figure 15. The damping time-scale of soil moisture estimated from the control experiment, the contour interval is 0.25 months.

itself long enough to have a substantial influence on the late summer rainfall. However, the initial rainfall anomaly propagation pattern does not depend qualitatively on whether soil moisture interacts with the atmosphere or not. The mechanisms for the initial rainfall anomaly propagation from the ocean onto the land are addressed below.

(*c*) *Role of radiation*

We now examine if the radiative processes are important to the initial propagation of the rainfall anomaly. We deliberately fix all the radiatively related variables to exactly the same values as in the control experiment, while imposing the same spring SST anomaly as in the standard anomaly experiment. The radiatively related quantities are atmospheric cooling rates and surface fluxes, including long-wave and short-wave components. In so doing, we do not allow the atmosphere to 'feel' the SST anomaly radiatively. The rainfall pattern is displayed in Fig. 16, which should be compared to the pattern in the control experiment (Fig. 11). We see that the essential pattern of rainfall anomaly remains. Furthermore, the rainfall anomaly in this experiment seems to last longer than that in the standard spring SST anomaly experiment, extending well into October. Physically, the internal atmospheric anomaly caused by the imposed SST anomaly is damped by the radiative response. When the atmosphere gets warmer, it emits more long-wave radiation and vice versa. Not allowing this negative feedback makes it difficult to get rid of the atmospheric thermal anomaly caused by the imposed SST anomaly. Therefore, it is not surprising that the rainfall anomaly lasts longer.

In summary, neither radiative processes nor soil moisture–rainfall feedbacks are essential for the initial rainfall anomaly propagation. Moreover, the rainfall anomaly propagation still exists even if we further turn off the wind–surface flux feedback, i.e. make the surface latent- and sensible-heat fluxes independent of wind speed. These numerical experiments will serve as the basis for our subsequent analysis.

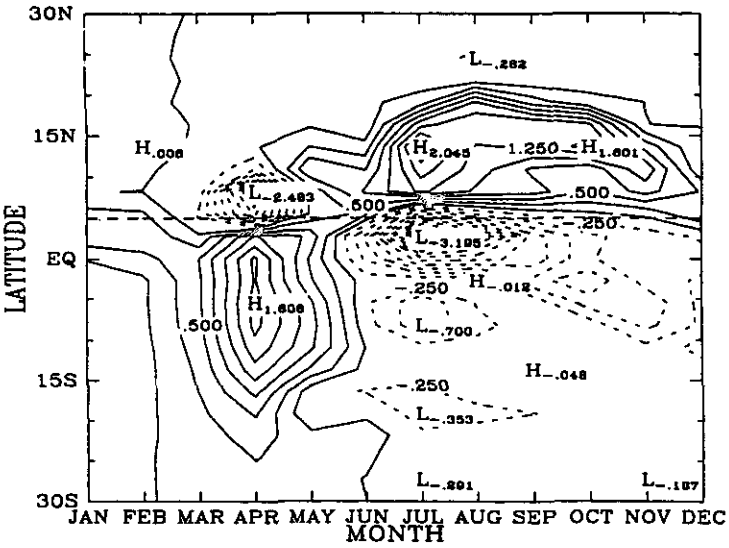

Figure 16. The total rainfall anomaly caused by the specified SST anomaly (magnitude of $T_{max} = 3.0$ K) for April–June. The radiation is fixed at the same values as in the control experiment. The contour interval is 0.25 mm day^{-1}.

(*d*) *Role of land surface temperature*

The rainfall anomaly pattern caused by the spring SST anomaly appears to be very robust, even if we fix both radiation and soil moisture as discussed above. The reason for the development of this rainfall anomaly pattern remains an open question.

The following experiment gives us some clues. By fixing the land surface temperature at the same values as in the control experiment, we can essentially shut down the rainfall anomaly pattern in the standard spring SST anomaly experiment (Fig. 17). This implies that whatever the mechanism is, it depends on interactive land surface temperature. This leads us to consider the land surface temperature evolution. For theoretical simplicity, we consider the case in which the surface net radiation and soil moisture remain unchanged. In addition, no wind–surface flux feedback is included. We know that the initial rainfall anomaly pattern does not depend critically on these constraints, as we have demonstrated through the numerical experiments. Therefore, the essential mechanisms for the development of the rainfall anomaly should not be affected by these assumptions. The land surface temperature perturbation can then be expressed as follows:

$$C_E \frac{\partial T_s'}{\partial t} = -L_v \bar{w} \rho_s C_D V_0 \{q_s(\bar{T}_s + T_s') - q_s(\bar{T}_s) - q_a'\} - C_p \rho_s C_D V_0 (T_s' - T_a'), \quad (8)$$

where quantities with overbars denote the control state and quantities with primes denote perturbations with respect to the control state. $\bar{w}$ is the relative soil saturation for the control state; ρ_s is the surface air density; C_D is the drag coefficient; V_0 is the surface wind magnitude; $q_s()$ is the surface saturation specific humidity for a given temperature; $\bar{T}_s$ is the land surface temperature for the control state; T_s' is the perturbation in land surface temperature; q_a' is the perturbation in surface air humidity, and T_a' is the perturbation in surface air temperature. Since T_s' is much smaller than $\bar{T}_s$, (8) can be approximated as:

$$C_E \frac{\partial T_s'}{\partial t} = -L_v \bar{w} \rho_s C_D V_0 \left(\frac{\partial q_s}{\partial \bar{T}_s} T_s' - q_a' \right) - C_p \rho_s C_D V_0 (T_s' - T_a'). \quad (9)$$

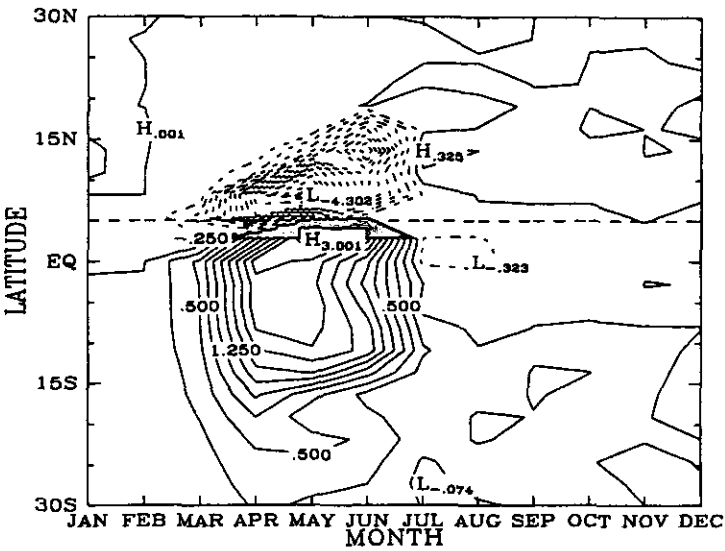

Figure 17. The total rainfall anomaly caused by the specified SST anomaly (magnitude of $T_{max} = 3.0$ K) for April–June. The land surface temperature is fixed at the same values as in the control experiment. The contour interval is 0.25 mm day^{-1}.

Using the Clausius–Clapeyron equation, we have:

$$\frac{\partial q_s}{\partial T_s} = \frac{L_v q_s}{R_v T_s^2}$$

where R_v is the gas constant for water vapour. Thus, (9) can be rewritten as:

$$\frac{\partial T_s'}{\partial t} = -\left(\frac{L_v^2 \bar{w} q_s}{C_p R_v T_s^2} + 1\right)\frac{T_s'}{\tau} + \left(\frac{L_v}{C_p}\bar{w}q_a' + T_a'\right)\frac{1}{\tau}, \tag{10}$$

where $\tau = \frac{C_E}{\rho_s C_D C_p V_0}$. For our model parameter values, $\tau \approx 5$ days. In other words, the land surface temperature damping time-scale is shorter than 5 days. On the other hand, the model rainfall anomaly (Fig. 11) and the accompanying land surface temperature anomaly pattern obviously have a much longer time-scale (~1 month). It appears that this longer time-scale can only be explained by the atmospheric anomalies caused by the imposed SST anomaly. The atmospheric anomalies (e.g. T_a' and q_a') can be viewed as forcing factors of the land surface temperature anomaly, as indicated by (10).

Since the land surface temperature damping time-scale (about 5 days) is much shorter than the rainfall anomaly propagation time-scale (~1 month), we can for simplicity assume zero heat capacity for the land surface. This gives us an instantaneous balance between the land surface temperature anomaly and the anomalies of near-surface atmospheric temperature and humidity (atmospheric forcings):

$$\left(\frac{L_v^2 \bar{w} q_s}{C_p R_v T_s^2} + 1\right) T_s' = \left(\frac{L_v}{C_p}\bar{w}q_a' + T_a'\right). \tag{11}$$

Equation (11) makes it clear that the time variation of the land surface temperature anomaly is dictated by the time variations of the atmospheric anomalies (T_a' and q_a') as long as the latter evolve over time-scales much longer than 5 days.

Rewriting (11) we have:

$$H'_a = C_p T'_a + L_v q'_a = \left(\frac{L_v^2 \bar{w} q_s}{C_p R_v T_s^2} + 1 \right) T'_s + (1 - \bar{w}) L_v q'_a, \tag{12}$$

where H'_a is the perturbation to the surface air moist static energy.

From its definition, we know that H'_a has essentially the same pattern as that of the perturbation of boundary layer entropy (θ'_e). Therefore, like θ'_e, H'_a also can be regarded as the key quantity in moist atmospheres. Now referring to (12), we see that H'_a is closely related to the land surface temperature perturbation T'_s, which in turn is closely related to atmospheric anomalies (see (11)). Since soil moisture has been proven not to be critical for the rainfall anomaly propagation, we consider the case in which the soil is saturated (like the ocean surface) so that H'_a is totally determined by T'_s. In fact, our experiments show that T'_s and T'_a have very similar spatial and temporal patterns. Furthermore, the magnitude of T'_a is generally smaller than that of T'_s. So if we assume that $T'_a = \gamma T'_s (0 < \gamma < 1)$, from (11) and (12) we have:

$$\frac{H'_a}{C_p} = \left\{ \frac{L_v^2 \bar{w} q_s}{C_p R_v T_s^2} + \frac{1 - \gamma(1 - \bar{w})}{\bar{w}} \right\} T'_s. \tag{13}$$

Now we see the importance of an interactive land surface temperature perturbation. Note, however, (13) is only a diagnostic relation, therefore we still do not know the cause of the land surface temperature and the boundary layer moist static energy perturbations.

In this section, we identified that the land surface temperature has to 'feel' the imposed SST anomaly for the rainfall anomaly propagation to occur. Since the time-scale of this propagation is of the order of one month or slightly smaller and the land surface temperature damping time-scale is less than 5 days, we concluded that the atmospheric anomalies must be the cause of the rainfall anomaly propagation. The land surface temperature almost instantly responds to changes of the near-surface atmospheric temperature and specific humidity (see (11)). The change of the land surface temperature then sustains the atmospheric anomalies caused initially by the SST anomaly. The ability of the underlying land surface to respond to the atmosphere is crucial for the rainfall anomaly propagation. In our hypothetical experiment, in which we artificially fixed the land surface temperature to the values of the control experiment, we essentially shut down this land–atmosphere interaction by assuming infinite land heat capacity, therefore the rainfall propagation pattern vanishes.

(e) *The atmospheric response to an SST anomaly*

The atmosphere over the ocean 'feels' the underlying SST almost immediately. This can be illustrated as follows. The SST anomaly influences the surface air moist static energy through turbulent fluxes. The change of the boundary layer moist static energy perturbation (H') due to surface fluxes can be expressed as:

$$\frac{\partial H'}{\partial t} = \frac{C_D V_0 (H'_s - H')}{\Delta z}$$

where $H'_s = C_p T'_s + L_v q'_s$ is the perturbation of oceanic saturation moist static energy due to the imposed SST anomaly, T'_s, and Δz is the depth of the boundary layer. All other notations were defined in the last section. Following derivations similar to those leading

to (10), we have:

$$\frac{\partial H'}{\partial t} = \frac{H'_s - H'}{\tau_0} = \frac{\left(C_p + \frac{L_v^2 \bar{q}_s}{R_v \bar{T}_s^2}\right) T'_s}{\tau_0} - \frac{H'}{\tau_0}. \tag{14}$$

The above equation can be rewritten as:

$$\frac{\partial \left(\frac{H'}{C_p}\right)}{\partial t} = \frac{1}{\tau_0}\left(1 + \frac{L_v^2 \bar{q}_s}{R_v \bar{T}_s^2}\right) T'_s - \frac{\frac{H'}{C_p}}{\tau_0}, \tag{15}$$

where $\tau_0 = \frac{\Delta z}{C_D V_0}$. This is the oceanic boundary layer air response time-scale to the imposed SST anomaly. For typical values: $\Delta z = 500$ m; $C_D \sim 10^{-3}$, $V_0 \sim 5$ m s^{-1}, we get $\tau_0 \sim 1$ day. Thus we see that the oceanic surface air responds to the imposed SST anomaly almost immediately, through turbulent mixing.

The nature and time-scale of the atmospheric response to an imposed SST anomaly can be examined more clearly using a simplified form of the model described earlier. The simplified model uses the same convective and radiative schemes, but consists of only two grid columns separated by a specified distance. A simple overturning circulation is driven by buoyancy gradients between the two columns, and no Coriolis effect is included. The overturning circulation is associated with vertical advection of moist static energy and water vapour in each column, and these quantities are also transported between columns by the horizontal branch of the circulation. On the other hand, the overturning circulation is not permitted to directly affect the surface fluxes for which a fixed surface wind is specified. The 'ocean' box has a fixed SST, while the lower boundary conditions for the 'land' box is an ocean of zero heat capacity, conventionally called a 'swamp'.

This simple model is first run into an equilibrium state with an ocean temperature fixed at a value less than that of radiative–convective equilibrium while the 'land'-box surface temperature is calculated using annual average solar radiation, interactive long-wave radiation, and surface fluxes. This leads to a land column that is warmer than the ocean column, and an associated 'monsoon' circulation with relatively large convective precipitation over land and small precipitation over ocean. The system reaches a steady state over several hundred days.

The steady solution is perturbed by suddenly increasing the ocean temperature by 2 K and then, 60 days later, decreasing it by 2 K. The effect of this on the precipitation in the 'land' box is shown in Fig. 18. At the onset of the SST anomaly, there is an immediate and dramatic reduction of precipitation, followed by a relaxation, over an approximately 30-day time-scale, back to values larger than those of the unperturbed state. At the time of cessation of the SST anomaly, there is an abrupt increase of the precipitation, followed by a slow relaxation to the unperturbed rate.

No positive rainfall anomaly occurs if the swamp temperature is fixed, as in the full model.

The vertical velocity at 600 mb in the 'land' box is shown in Fig. 19. After an abrupt decrease, the upward motion slowly relaxes back to values slightly less than those of the unperturbed state. The cessation of the SST anomaly causes an abrupt increase of vertical velocity, followed by a decaying oscillation of period near 40 days.

Detailed analysis of these simulations using the simple model reveals the physics governing the model behaviour. When the SST anomaly is switched on, the warmth of the sea surface is quickly communicated to the atmosphere by convection, and the monsoon circulation quickly reacts by slowing down. The time-scale of this response is of order 1 day, and leads to a comparably fast diminution of convective rainfall over land. At the same

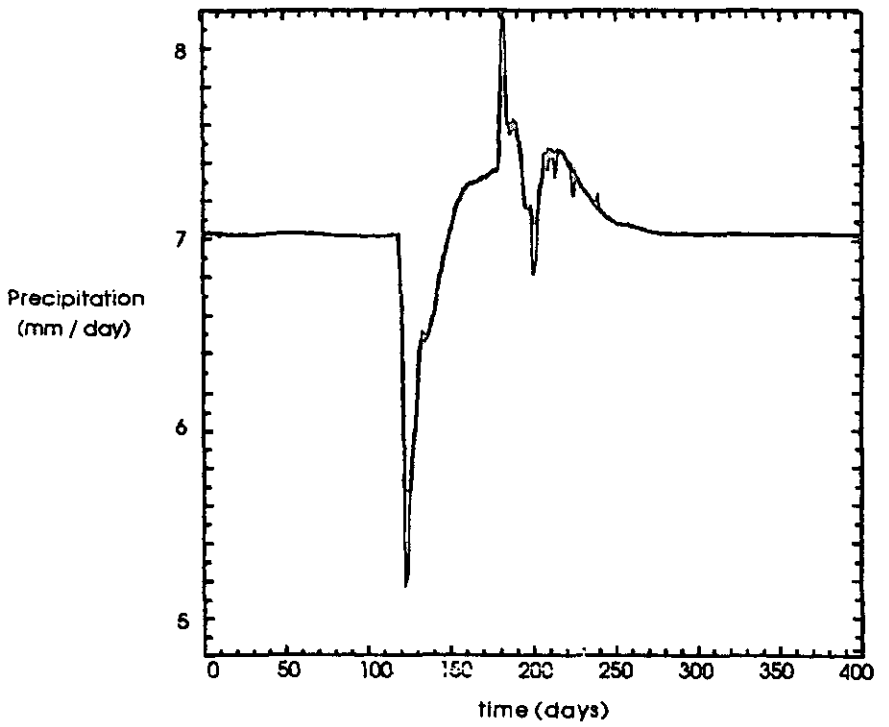

Figure 18. The time evolution of precipitation (mm day^{-1}) in the 'land' box (see text) for the double-column model. The ocean temperature perturbation is switched on at day 120, and switched off at day 180.

time, the SST anomaly quickly leads to an anomaly of precipitable water over the ocean, which, by virtue of the concentration of water vapour in the lower troposphere, is advected landward in the lower branch of the monsoon. This gradually increases the precipitable water over land, over an advective time-scale which in this case is about 20 days. This restores the precipitation to values that are actually slightly larger than the unperturbed precipitation rate; i.e. the additional moisture overwhelms the effect of reduced ascent.

Then, when the SST anomaly is removed, there is quick acceleration of the monsoon circulation and, for a period of about 30 days, the land enjoys exceptionally large precipitation, owing to the conjunction of large ascent and large precipitable water left over from the moisture advected landward from the vicinity of the now defunct SST anomaly. Gradually, again over an advective time-scale, the moisture anomaly diminishes and the precipitation returns to its unperturbed value.

Note, however, that this simple picture is blemished by a negative precipitation anomaly that occurs about 20 days after the SST anomaly is shut down. This is associated with the damped oscillation of the vertical velocity referred to earlier. Analysis of the model shows that this oscillation is a form of damped internal gravity wave (or, more precisely, its two-column equivalent), whose physics is similar to that described in Emanuel *et al.* (1994). There is little evidence of such an oscillation in the full model, probably because in that case the SST anomaly was *gradually* increased and decreased in time, rather than being suddenly switched on and off.

Finally, it is worth noting that in a similar experiment but with fixed radiation, the model behaviour is similar, except that the negative precipitation anomaly in the 'land' box

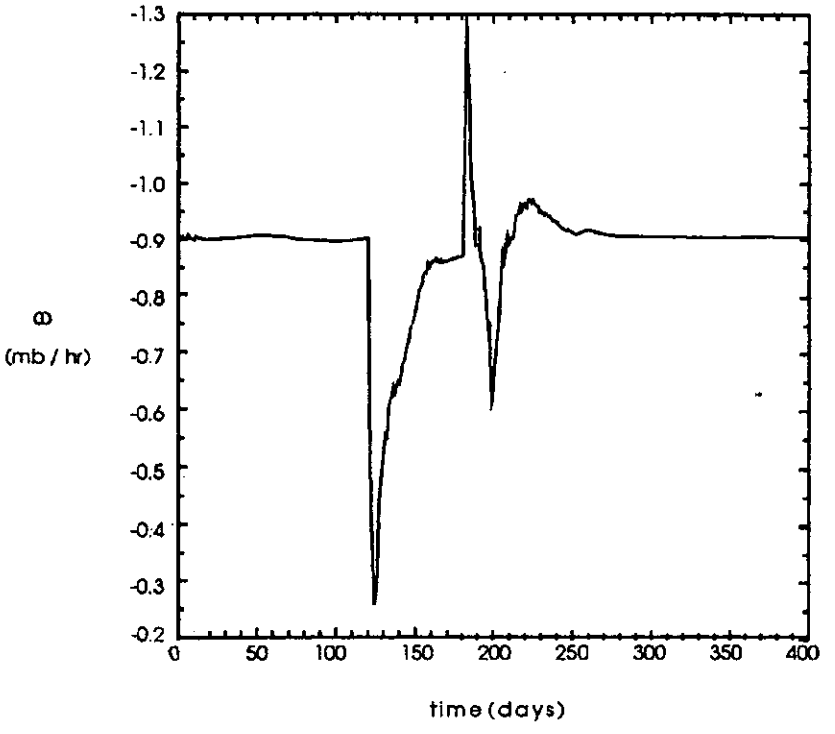

Figure 19. The time evolution of pressure vertical velocity at 600 mb in the 'land' box (see text) for the double-column model. Note that negative values indicate upward motion.

does not reverse sign before the SST anomaly is switched off, as it does in the case with interactive radiation. This reveals an interesting radiative feedback in the system. When the SST-induced moisture anomaly is advected over land, the additional greenhouse forcing by the water vapour increases the land surface temperature, which almost entirely mitigates the reduction of the monsoon circulation and also increases the surface evaporation rate. The resulting monsoon is only slightly reduced from the unperturbed state, but this reduction is more than compensated by the increased moisture imported from the sea; as a result, the precipitation rate is actually greater than in the unperturbed state.

4. Comparison of observations between 1994 and 1992

In this section, we present a case-study comparing 1992 with 1994. Our emphasis here is to identify patterns of the difference of various variables between the two years. The reasons for choosing 1992 and 1994 are as follows. First, 1992 is the driest year and 1994 the wettest year in the 1990s; so that we are comparing the driest and the wettest years in the 1990s so far. Secondly, the ECMWF methods of analysing data are never homogeneous owing to the constant updating of the ECMWF model. By choosing relatively close years, this problem may be partially avoided. Thirdly, the long-term effect of land-cover transformation such as deforestation and desertification may also be minimized due to the closeness of 1992 and 1994 (this does not mean that the short-term land surface conditions such as soil moisture are the same for the two years). Most importantly, the spring SST conditions in 1992 are significantly different from the corresponding conditions

in 1994. This is important since these observations will be discussed in the light of the mechanism proposed in previous sections.

(*a*) *Rainfall*

The rainfall dataset we use here is that of the Global Precipitation Climatology Project (GPCP). This provides monthly mean 2.5 × 2.5 gridded precipitation data for July 1987 through November 1994 (December of 1994 is missing). The dataset has been produced by blending rain-gauge analysis, satellite-derived (infrared and microwave) estimates of precipitation and National Weather Prediction model precipitation information (Huffman *et al.* 1995). The dataset uses rain-gauge analysis wherever possible. The gauge data are analyses from the Global Precipitation Climatology Centre, and reflect approximately 6700 gauges which have been carefully selected by applying a quality control system.

The GPCP dataset is used to identify the pattern of the rainfall difference between 1994 and 1992. Figure 20 describes the annual mean rainfall from 30°S to 30°N and from 25°W to 25°E for 1994 (Fig. 20(a)), 1992 (Fig. 20(b)) and the difference between 1994 and 1992 (Fig. 20(c)). We see that the annual rainfall in 1994 is larger than that in 1992 over the whole west African region (defined as the region from 15°W to 15°E), by a magnitude ranging from 50 mm to 300 mm. Note that the African southern Atlantic coast is around 5°N. By averaging rainfall longitudinally from 15°W to 15°E, Fig. 21(a) and 21(b) depict the seasonal migration of rainbelts for 1994 and 1992 respectively. Figure 21(c) shows the difference between 1994 and 1992. We observe that the larger annual rainfall over west Africa is mainly due to the positive rainfall anomaly from July through November, reaching a maximum in September and October (~2.0–2.5 mm day^{-1}). October of 1994 is quite unusual in terms of the rainfall anomalies, because often October is near the end of the Sahel rainy season. The unusually abundant rainfall in October of 1994 is associated with the fact that the ITCZ maintains a northward position for an anomalously long period of time in that year (see Fig. 21(a) and (b)). Note also that the rainfall over land is actually less in 1994 from May to July. At the same time, over the ocean we observe heavier rainfall. This spring positive rainfall anomaly pattern over the ocean follows a positive rainfall anomaly from January to February and a negative rainfall anomaly from February to April, over all the ocean and coastal regions.

(*b*) *SST*

The SST data used here are taken from the monthly OI SST analysis, which uses in situ observations and satellite-derived SSTs (Reynolds and Smith 1994). The in situ data were obtained from radio messages carried on the Global Telecommunication System. The satellite observations were obtained from operational data produced by the National Environmental Satellite Data and Information Service. The data cover the whole globe and have a spatial resolution of 1° × 1°. The time coverage is from January 1981 to December 1995.

Figure 22 shows the longitudinally averaged (15°W to 10°E) SST difference between 1994 and 1992. We see that in general the SST in 1994 is higher than that in 1992. Other features should be pointed out. First of all, the positive SST anomaly dominates from April to June and reaches a maximum of 1.5 degC in May. Secondly, the summer SST (from July to September) is also higher in 1994 but the magnitude is only around one-third of the spring SST difference. This SST-difference pattern agrees with that estimated by Lamb (1978b; see his Fig. 5 and Fig. 6) in the spring SST difference between the wet and dry composites, but differs from that of his summer SST difference. As has been demonstrated in previous sections, the spring SST may have an important influence on west African rainfall.

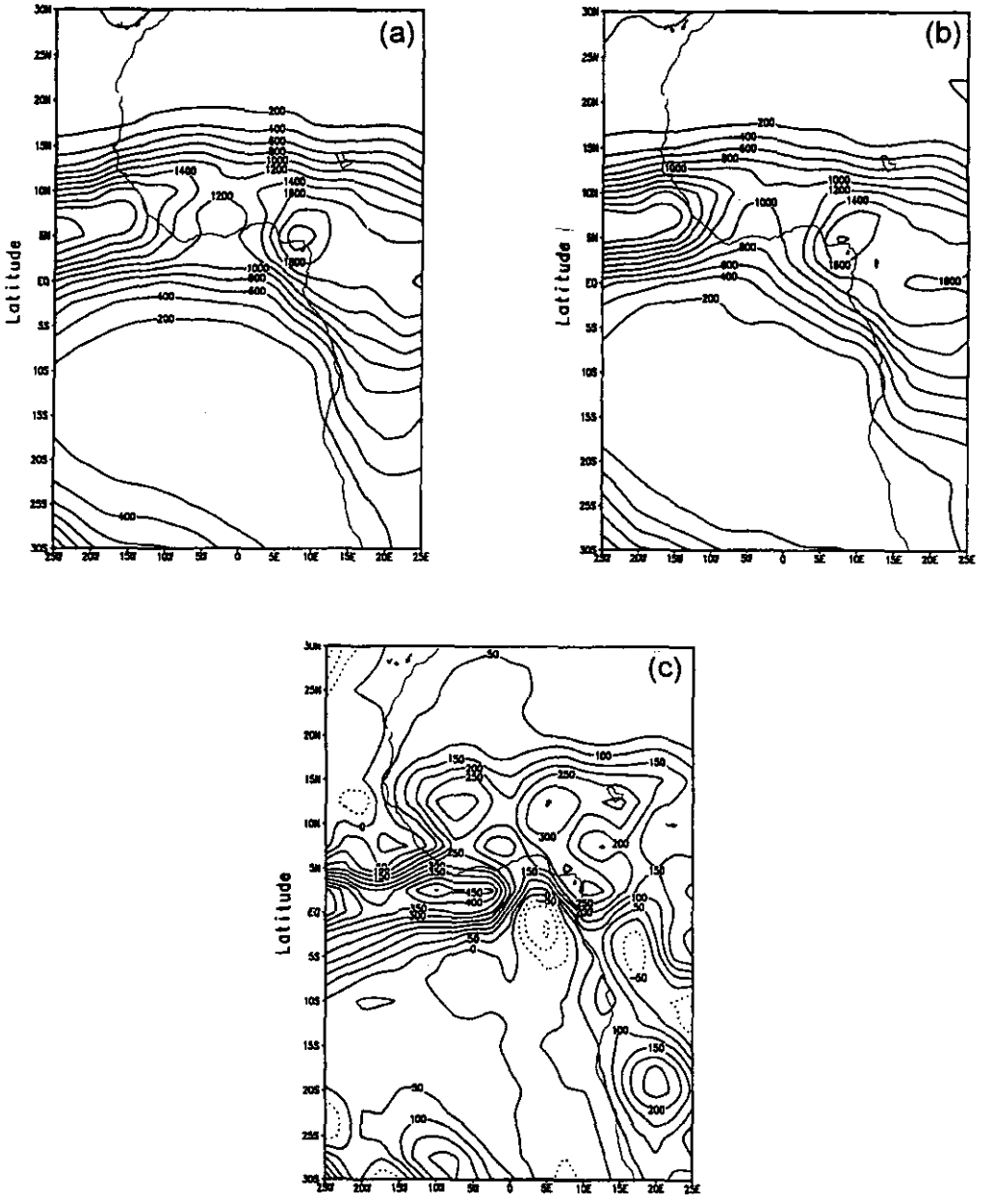

Figure 20. The annual mean rainfall (mm) in the region from 25°W to 25°E and from 30°S to 30°N for (a) 1994, (b) 1992 and (c) 1994 − 1992 (dashed lines are negative). The contour intervals are 100 mm for (a) and (b), and 50 mm for (c). Data are from the GPCP (see text) rainfall dataset.

(*c*) *Wind*

We use the ECMWF dataset, with spatial resolution 2.5° × 2.5°. The data extend from January 1985 to December 1995, with two observations available every day: 0000 UTC and 1200 UTC. We use the monthly average, and also average the data over day and night. During this eleven-year period, the method used to analyse the observational data has been updated several times, so the dataset is not homogeneous. However, for the years

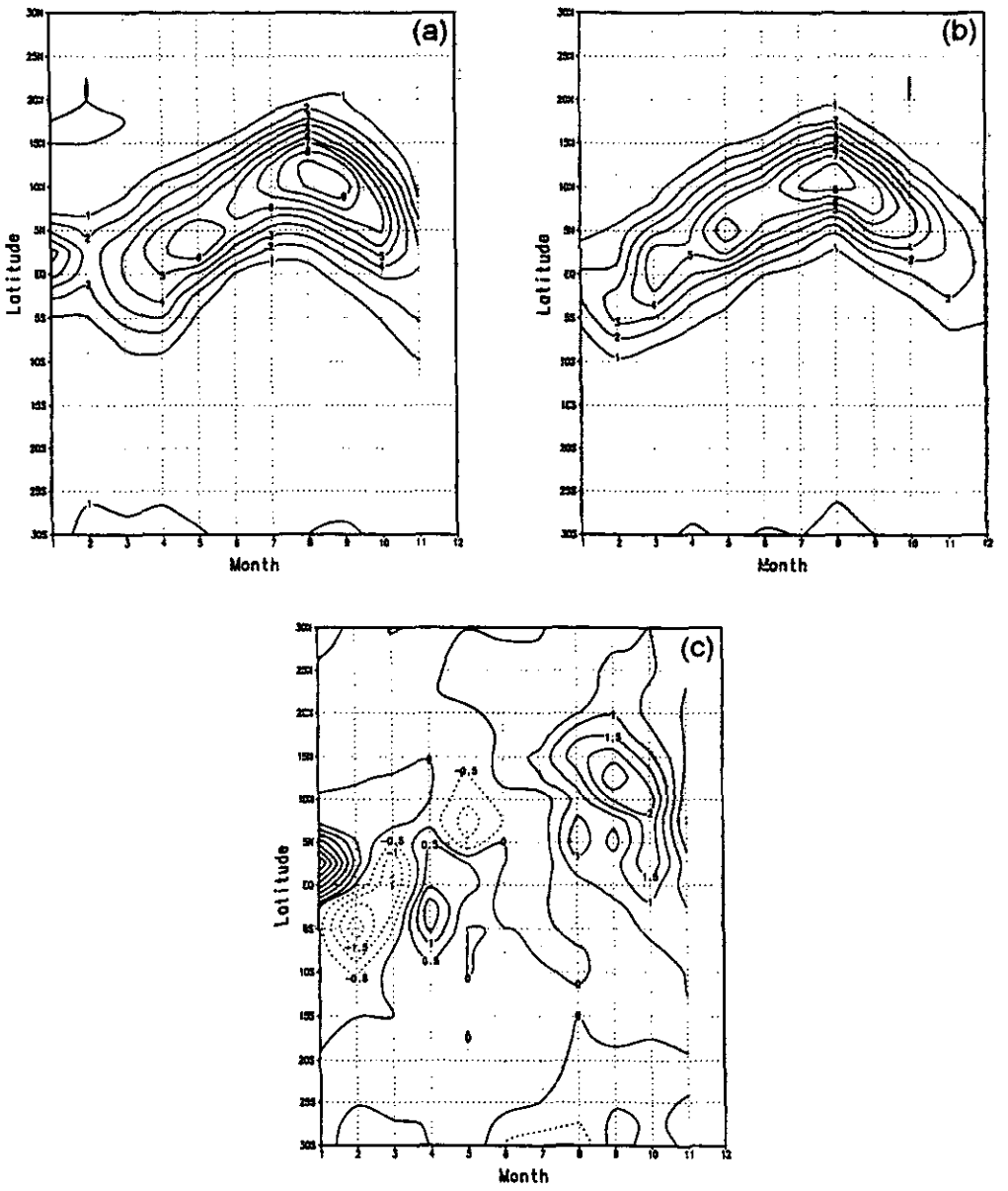

Figure 21. Longitudinally averaged (from 15°W to 15°E, west African region) rainfall latitude–month cross-sections for (a) 1994, (b) 1992 and (c) 1994 − 1992 (dashed lines are negative). The contour intervals are 1 mm day^{-1} for (a) and (b), but 0.5 mm day^{-1} for (c). Note that rainfall data for December 1994 are missing.

of interest, 1992 and 1994, we can reasonably assume homogeneity during this relatively short period of time.

The meridional wind for the summer months shows strong southerlies near the surface, and northerlies near the tropopause for both 1994 and 1992 (Fig. 23). The picture agrees with the notion that west African monsoons can be viewed as thermally direct meridional circulations (e.g. Plumb and Hou 1992; Zheng and Eltahir 1997). The difference between the meridional wind in these two years (Fig. 23(c)) indeed shows a stronger meridional

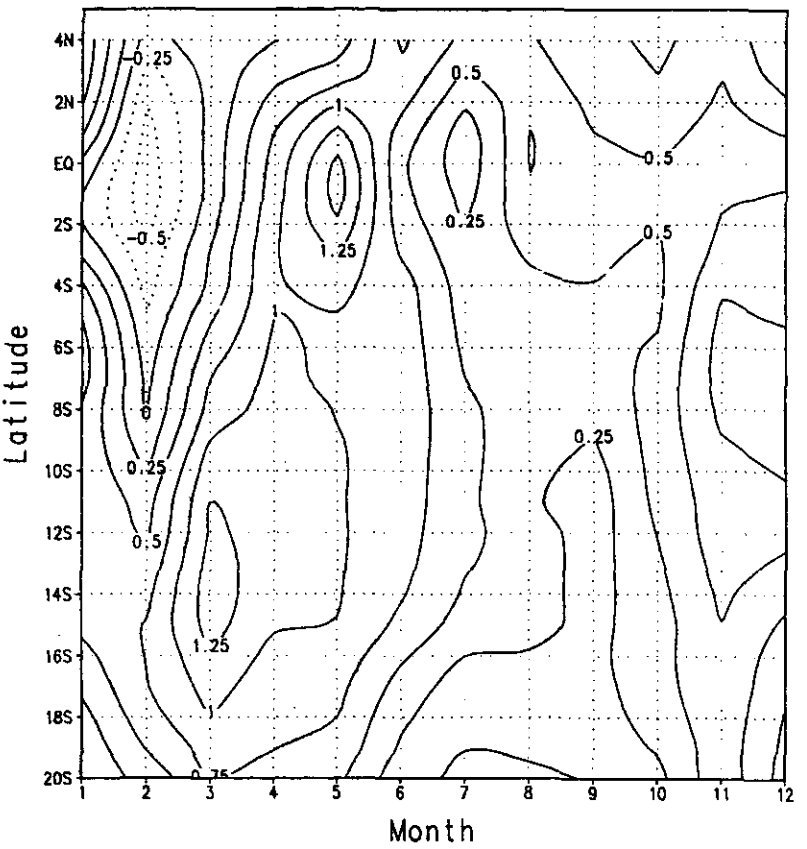

Figure 22. The longitudinally averaged (from 15°W to 10°E) SST difference between 1994 and 1992. The contour interval is 0.25 degC.

circulation in 1994. In addition, the low-level southerly extends further northward in 1994. As we have seen from the rainfall analysis, October of 1994 is very exceptional. Therefore, we single out the month of October here (Fig. 24). The low-level southerly wind extends up to 15°N in October of 1994 but only up to 12°N in 1992. Again, Fig. 24 indicates stronger October meridional circulation in 1994. Furthermore, the anomalous southerlies are very deep in October (up to 400 mb). These anomalies are not only deeper but also stronger than those of the summer months (Fig. 23(c) and Fig. 24(c)).

The zonal wind shows a stronger upper-level easterly jet (not shown) and stronger surface wind (not shown) in 1994. In addition, the low-level easterly jet in the northern hemisphere (15°N) is stronger during the dry year of 1992. This in general agrees with the analyses by Newell and Kidson (1984) for their wet (1958–1963) and dry (1969–1973) composites.

Finally, the horizontal divergence (Fig. 25) near the tropopause (250 mb) displays a good correspondence with the rainfall pattern (Fig. 21). The upper-level divergence pattern should reflect that of the vertical motion which in turn is closely related to rainfall. A positive rainfall anomaly should be associated with a positive upper-level divergence anomaly. The difference in the upper-level divergence between 1994 and 1992 is given by Fig. 25(c). Comparing with Fig. 21(c), we observe a resemblance between the two.

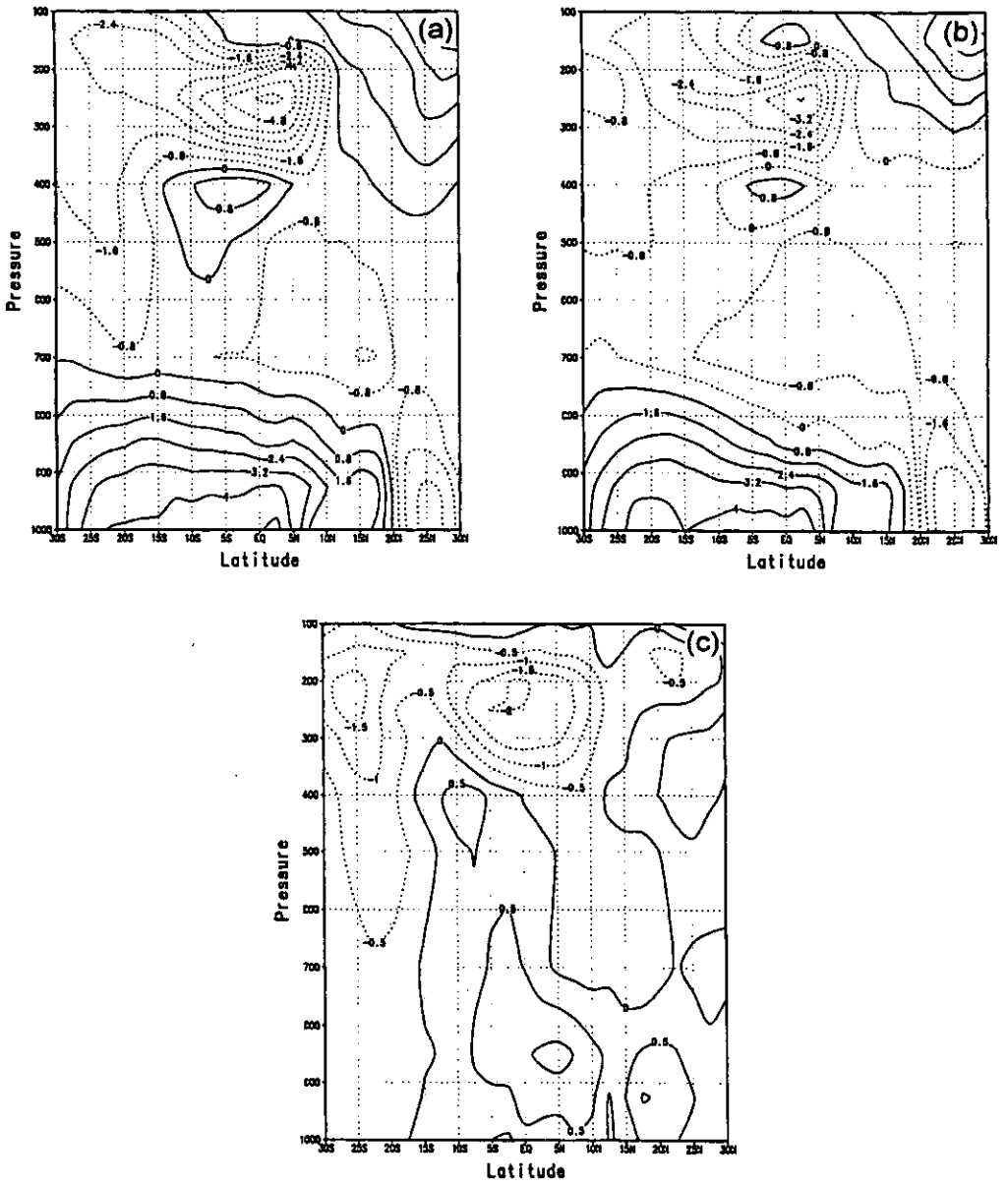

Figure 23. The longitudinally averaged (from 15°W to 15°E) summer (July–September) meridional wind pressure–latitude cross-section for (a) 1994, (b) 1992 and (c) 1994 − 1992 (dashed lines are negative). The contour intervals are 0.8 m s^{-1} for (a) and (b), but 0.5 m s^{-1} for (c).

Notice the migration of the positive divergence belt from the ocean onto land as the season progresses. The positive anomalous divergence seems to originate in April and May and then propagates onto the land, reaching a maximum in September and October, roughly agreeing with rainfall anomalies. The negative anomalous divergence persists from April to June over the land area from about 5°N to 17.5°N, consistent with the deficient rainfall over the land during the same period of time as shown in Fig. 21(c).

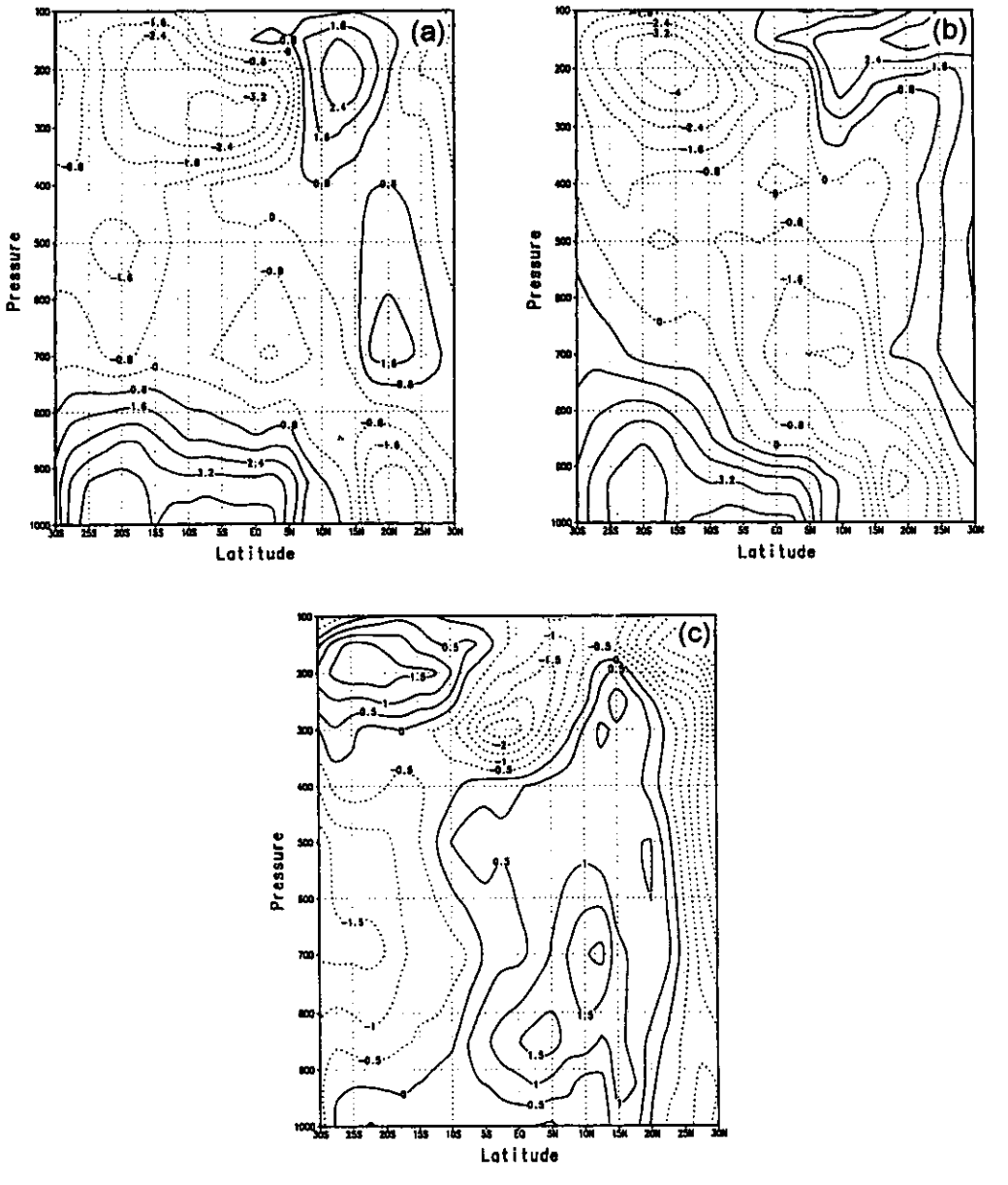

Figure 24. As Fig. 23 but for October.

(*d*) *Boundary layer entropy*

Emanuel (1994, 1995) and Emanuel *et al.* (1994) argued for the critical importance of boundary layer entropy in the dynamics of moist atmospheres. Moreover, Eltahir and Gong (1996) pointed out the important role of boundary layer entropy in the dynamics of west African monsoons. Therefore, we present here some analyses of boundary layer entropy (expressed as θ_e), averaged over the two lowest pressure levels, 1000 mb and 925 mb. As we can see in Fig. 26(c), which is the difference between 1994 and 1992, θ_e over the

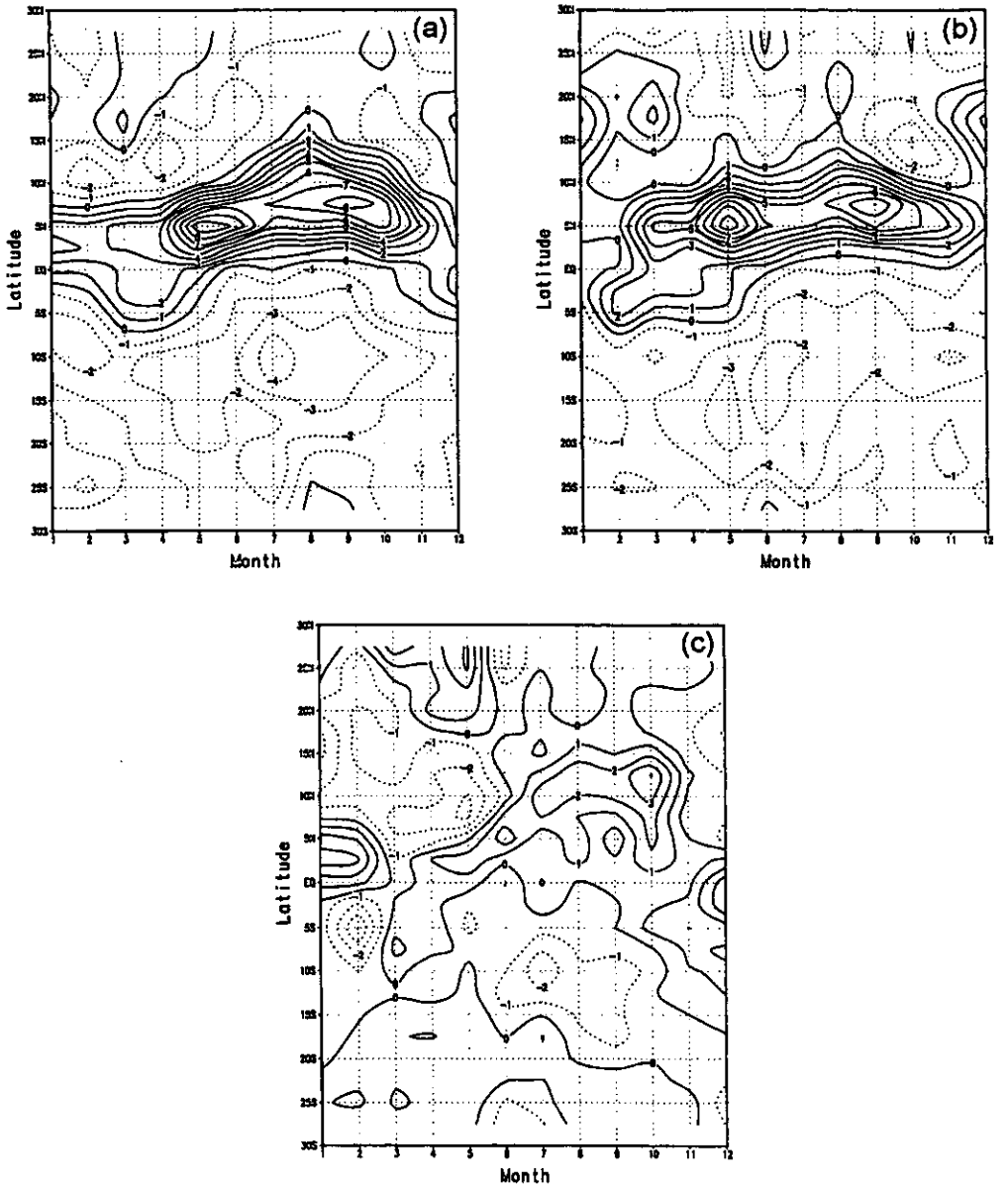

Figure 25. The longitudinally averaged (from 15°W to 15°E) horizontal divergence (250 mb, units $10^{-6}s^{-1}$) for (a) 1994, (b) 1992 and (c) 1994 − 1992. The contour interval is $1 \times 10^{-6}s^{-1}$.

ocean is generally higher in 1994 than in 1992, except during January and February. This is consistent with the SST-difference pattern (Fig. 22). This also confirms the notion that the boundary layer θ_e over the ocean basically follows the SST. What is striking in Fig. 26(c) is that over the land area the boundary layer θ_e exhibits large differences between the two years. In particular, a positive anomaly of θ_e starts to build up in June and reaches a maximum in October, consistent with both the rainfall anomaly pattern (Fig. 21(c)) and the upper-level divergence pattern (Fig. 25(c)). In fact, before the onset of the strong rainfall

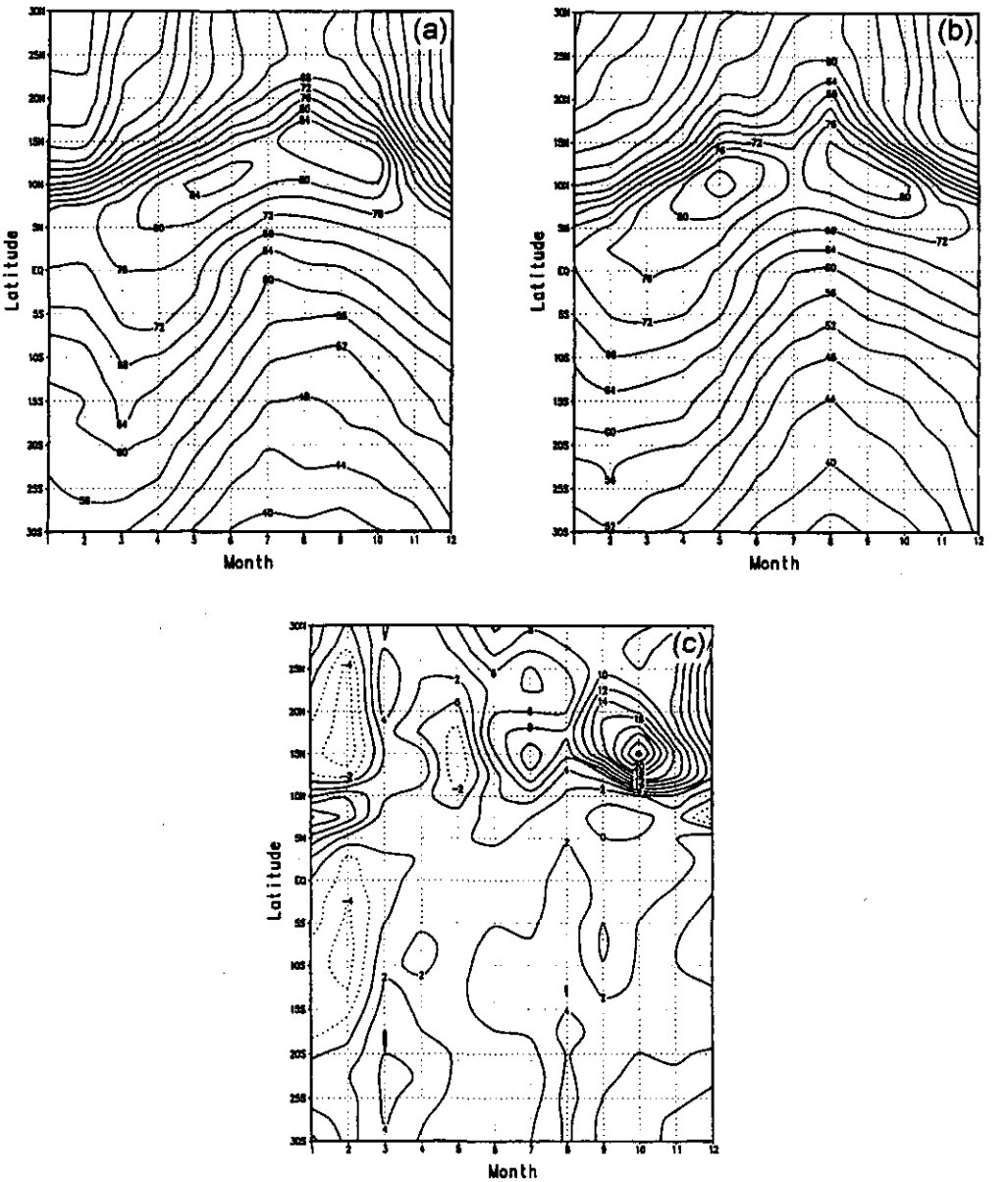

Figure 26. The boundary layer equivalent potential temperature, θ_e in °C, averaged from 15°W to 15°E and 1000 mb to 925 mb for (a) 1994, (b) 1992 and (c) 1994 – 1992. The contour intervals are 4 degC for (a) and (b) but 2 degC for (c).

over Sahel, the boundary layer θ_e shows a substantially stronger meridional gradient in 1994 than in 1992 (Fig. 27). Similar results were obtained by Eltahir and Gong (1996) in their analysis of the 1958 wet year and the 1960 dry year. Another notable difference pattern of boundary layer θ_e is the negative anomaly for the month of May over the Sahel region (10°N to 20°N), coinciding with the rainfall difference pattern. The positive boundary layer θ_e anomaly over the land area is mainly associated with a positive specific humidity anomaly, as can be seen in Fig. 28. The surface air temperature is higher during spring (up

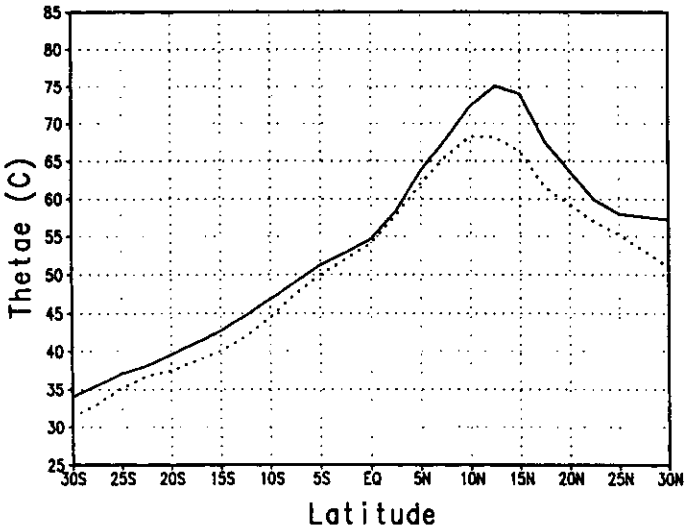

Figure 27. The latitudinal profile of boundary layer equivalent potential temperature θ_e (°C) averaged from 15°W to 15°E and 1000 mb to 925 mb for July 1994 (solid line) and July 1992 (dotted line).

to June) but lower for the rainy season, presumably due to larger evaporation caused by heavier rainfall in 1994 (Fig. 29).

(*e*) *Summary*

The above analyses reveal remarkable consistencies among rainfall, wind and boundary layer entropy despite independent sources of data. It appears that the 1994 wet year in west Africa is closely associated with a stronger monsoon in 1994 than in 1992. The rainfall anomaly pattern in Fig. 21(c) and the upper-level divergence anomaly pattern of Fig. 25(c) are very similar, showing the migration of the anomaly from ocean during the spring onto the continent during the summer. The April to May positive rainfall anomaly over the ocean is loosely consistent with the high SST at that time (Fig. 22). These observations are consistent with the mechanism proposed in the previous section. This leads us to speculate that the spring SST anomaly may have been important in shaping the observed interannual variability of rainfall over west Africa, at least for some years.

5. Summary and conclusions

We have attempted to determine the nature of and reason for the influence of SST anomalies on the west African monsoon. We used a two-dimensional numerical model with interactive radiation, convection, and land surface properties to investigate the physical nature of the relationship between SST anomalies and rainfall over land. Seasonally varying solar radiation and sea surface temperatures drive the circulation in the model. During summer, the relatively warm equilibrium conditions over land drive a monsoon with low-level flow from ocean to land. When a pattern of SST anomalies is superimposed during spring, there is a noticeable diminution of rainfall over land concomitant with a positive SST anomaly, but enhanced rainfall occurs in the following summer and early autumn. This lagged response to imposed SST anomalies seems to be especially strong when the anomalies are imposed in spring, supporting the suggestion by Owen and Ward (1989) that spring SST can be used to predict summer rainfall. The reason behind this in the

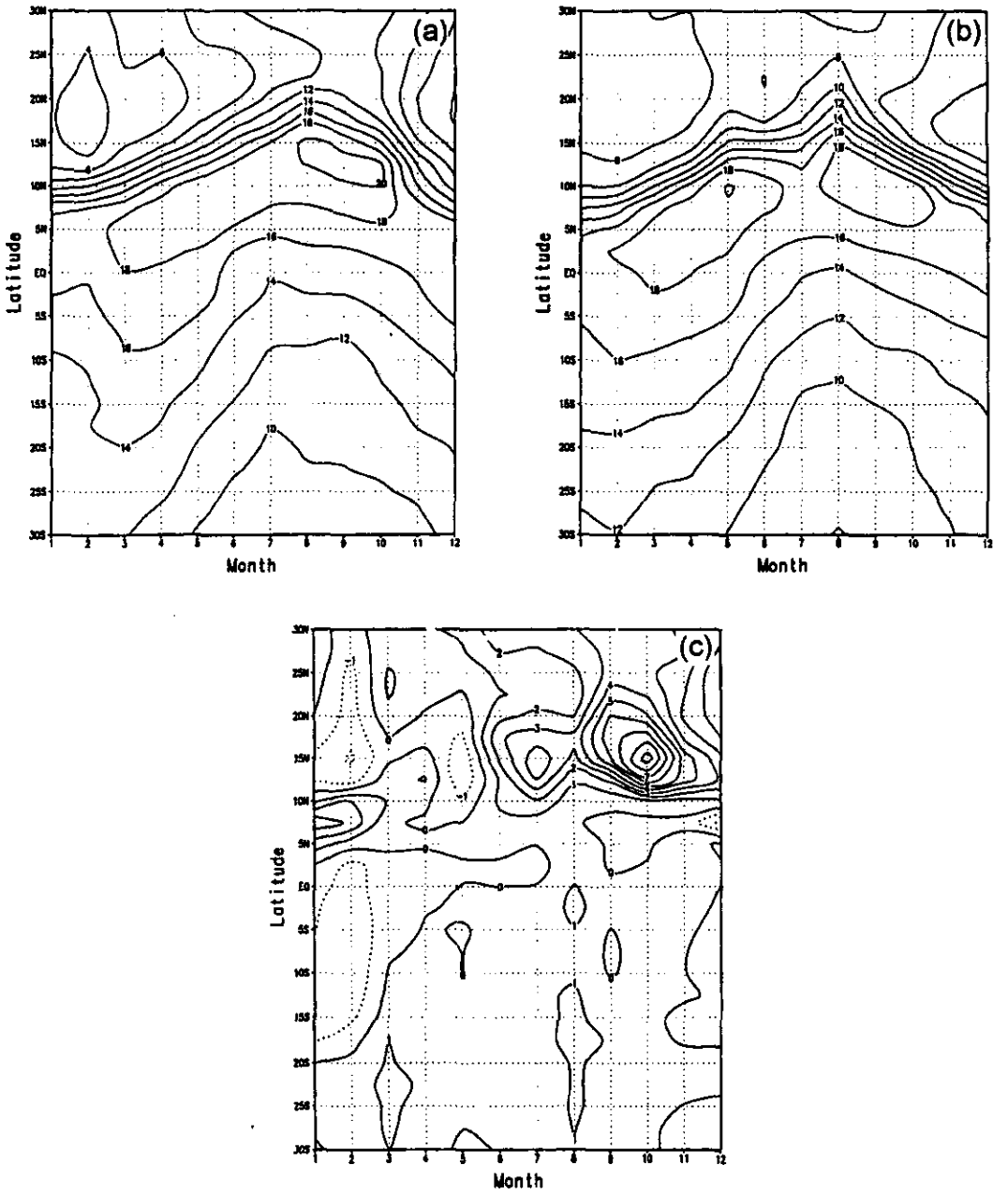

Figure 28. As Fig. 26 but for specific humidity (g kg^{-1}), with contour intervals 2 g kg^{-1} for (a) and (b) but 1 g kg^{-1} for (c).

control experiment is that the timing of spring SST anomalies coincides with the onset of the monsoon.

A detailed analysis of the simulations made using the two-dimensional model, and using a double-column model, reveals the basic physical mechanisms underlying the model's behaviour. The rapid warming of the maritime atmosphere resulting from the imposed positive SST anomaly very quickly reduces the strength of the monsoon flow, owing to the

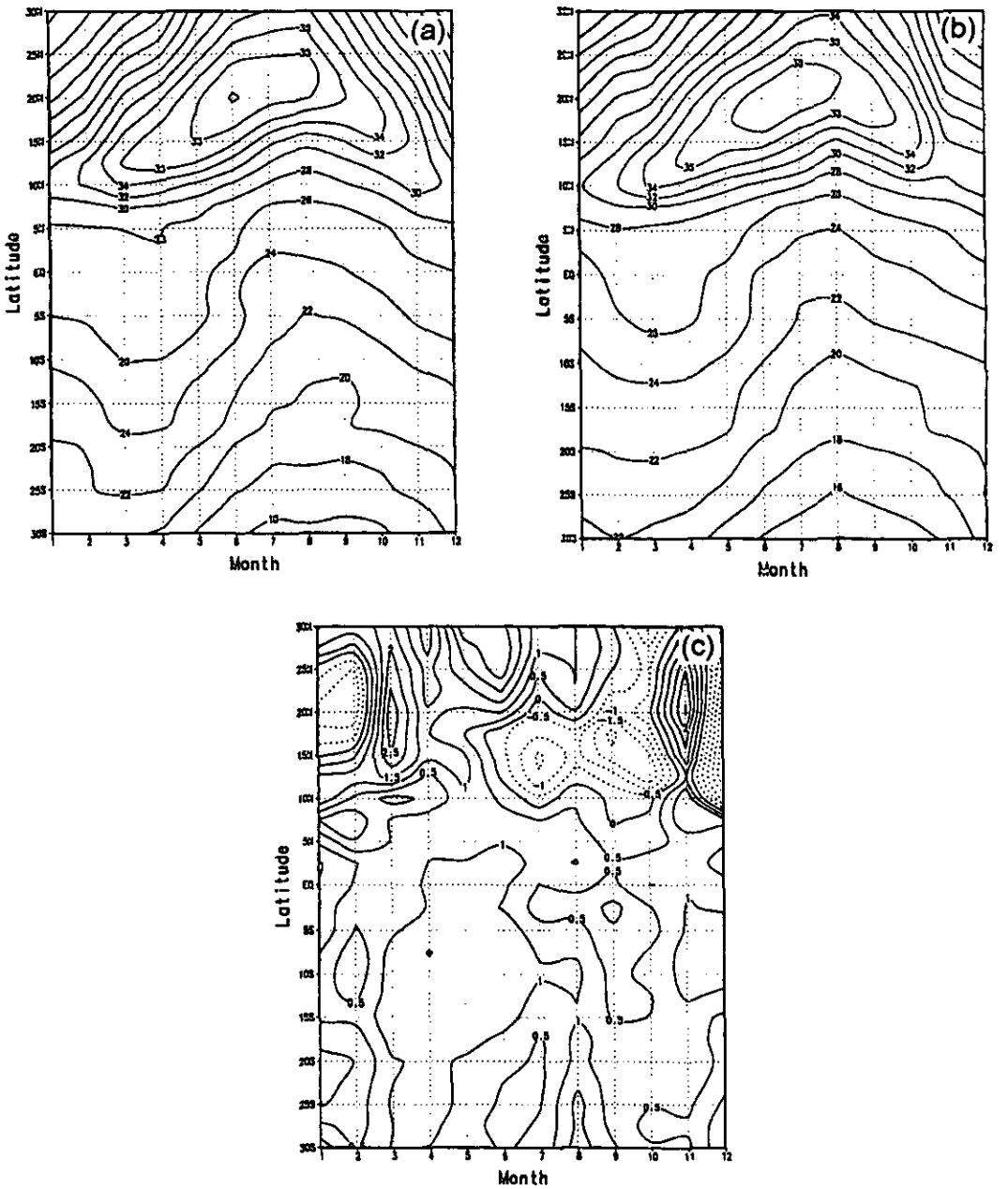

Figure 29. As Fig. 26 but for temperature in °C, with contour intervals 2 degC for (a) and (b) but 0.5 degC for (c).

reduced atmospheric density gradient between ocean and land. The immediate result of this is reduced precipitation over land. But over a time-scale dictated by advection by the large-scale circulation (in this case about 20 days), the precipitation anomaly over land reverses and becomes positive. There are two basic reasons for the initial enhancement of precipitation: first, the anomalous moisture over the ocean is advected inland; second, the increased moisture over land leads to increased greenhouse trapping, raising the temper-

ature of the air over land, which in turn restores the strength of the monsoon flow. Then, when the imposed SST anomaly is removed, the rainfall becomes large over land, owing to the conjunction of the restored basic monsoon flow, the enhancement of the monsoon by anomalous greenhouse trapping over land, and the anomalous precipitable water. These last two effects are vestiges of the SST anomaly and gradually disappear over the monsoon advective time-scale of around 20 days.

Fixing the soil temperature while imposing the SST anomaly results in no substantial enhancement of precipitation over land. This is because fixing the surface temperature is tantamount to inserting an infinite heat capacitor in the system, preventing the boundary layer entropy from increasing by advection.

Interactive soil moisture was found to be crucial to prolong substantially the anomalous summer rainfall, through it is not essential for the initial rainfall enhancement over land. The positive soil moisture–rainfall feedback sustains the initial rainfall anomaly, and the rainfall anomaly persists two to three months even after the disappearance of the SST anomaly. We emphasize the importance of radiative and dynamical processes in the positive soil moisture–rainfall feedback.

We stress that the time-scale of order 20 days of the monsoon flow is essential in explaining the lagged response of rainfall over land to imposed SST anomalies. The 20-day value should not be sensitive to horizontal scales associated with the monsoon; it is, fundamentally, the time-scale of air sinking through the troposphere under the influence of radiative cooling. Larger horizontal scales of the monsoon will be associated with larger horizontal flow speeds, while the vertical motion is limited by the radiative cooling rate.

Our study here has some important implications. As we reviewed in section 1, most previous studies (although not all of them) of the influence of SST on west African rainfall focus on the statistical correlation between summer SST and summer rainfall, and therefore do not elucidate any causal relationships between the two. This study, although not conclusive, points to the potential importance of spring SST anomalies for summer rainfall, and thus provides some theoretical basis for using spring SST to predict summer rainfall. Furthermore, we found that three-way interactions between ocean, land, and atmosphere are responsible for this connection between spring SST anomaly and summer rainfall. This suggests that local land surface forcing and remote oceanic SST forcing should not be considered separately, as far as the west African rainfall variability is concerned.

Comparing the dry year of 1992 with the wet year of 1994 suggests that springtime SST anomalies in the equatorial Atlantic, south of west Africa, may have an important influence on summer and early autumn rainfall in west Africa. The remarkable consistency among various independent datasets suggest that this result is robust. However, our study here has not yet demonstrated that the observed SST anomalies such as shown in Fig. 22 can indeed force the observed rainfall anomalies shown in Fig. 21. In fact, our model-simulated rainfall anomalies (not shown here) caused by the observed SST anomalies (Fig. 22) are one order of magnitude smaller than observed (Fig. 21), although the rainfall anomaly patterns bear some resemblance, propagating from ocean onto land. It appears that our model is less sensitive to boundary layer forcing, probably reflected in substantial differences between the model boundary layer entropy and that of the observations. In general, the crucial importance of boundary layer entropy in the dynamics of moist atmospheres (Emanuel 1994, 1995; Emanuel *et al.* 1994; Eltahir and Gong 1996) suggests that we may need to use boundary layer entropy as an index in evaluating the model control climate against the observations. Most modelling studies, including our study here, simply compare model controlled rainfall distribution with observations. Our failure to obtain a more realistic model controlled boundary layer entropy may contribute to the relative insensitivity of our model rainfall to SST forcing.

Finally, our analysis in this paper simply points out one possible mechanism of west African rainfall variability, which is often ignored. There are many other mechanisms that may be responsible for west African rainfall anomalies. For example, the role of summer tropical Atlantic SST anomalies and global SST teleconnections have been investigated in much more detail, as well reviewed in section 1. Spring SST anomalies may be important for west African rainfall variability for a particular year (e.g. 1994) but perhaps not in other years. Our study demonstrates an additive, potentially important mechanism for west African droughts and floods.

ACKNOWLEDGEMENTS

Xinyu Zheng would like to thank Dr Alan Plumb for his support throughout the course of this study. Guiling Wang is thanked for providing the data used in this study. Eltahir research is supported through an NSF grant ATM-9807068.

REFERENCES

Budyko, M. I. 1974 *Climate and life*. International Geophysical Series, volume 18, Academic Press, New York, USA

Charney, J. G. 1975 Dynamics of desert and drought in the Sahel. *Q. J. R. Meteorol. Soc.*, **101**, 193–202

Charney, J. C., Stone, P. H. and Quirk, W. J. 1975 Drought in the Sahara: a biogeophysical feedback mechanism. *Science*, **187**, 434–435

Charney, J. G., Quirk, W. J., Chow, S.-H. and Kornfield, J. 1977 A comparative study of the effects of albedo change on drought in semi-arid regions. *J. Atmos. Sci.*, **34**, 1366–1385

Chou, Ming-Dah, Dratz, D. P. and Ridgway, W. 1991 Infrared radiation parameterizations in numerical climate models. *J. Climate*, **4**, 424–437

Cunnington, C. and Rowntree, P. R. 1986 Simulations of the Saharan atmosphere dependence on moisture and albedo. *Q. J. R. Meteorol. Soc.*, **112**, 971–999

Darnell, W. L., Staylor, W. F., Gupta, S. K., Ritchey, N. A. and Wilber, A. C. 1995 A global long-term data set of shortwave and longwave radiation budget. *GEWEX News*, **4**, No. 3, 1–8

Delworth, T. L. and Manabe, S. 1988 The influence of potential evaporation on the variabilities of simulated soil wetness and climate. *J. Climate*, **1**, 523–547

Dickinson, R. E., Henderson-Sellers, A., Kennedy, P. J. and Wilson, M. F. 1986 'Biosphere Atmosphere Transfer Scheme (BATS) for the NCAR Community Climate Model'. Tech. Note 275f STR, NCAR, Boulder, CO, USA

Druyan, L. M. and Hastenrath, S. 1991 Modelling the differential impact of 1984 and 1950 sea surface temperature on Sahel rainfall. *Int. J. Climatol.*, **11**, 367–380

Eltahir, E. A. B. 1998 A soil moisture–rainfall feedback mechanism. 1: Theory and observations. *Water Resources Research*, **34**(4), 765–776

Eltahir, E. A. B. and Gong, C. 1996 Dynamics of wet and dry years in West Africa. *J. Climate*, **9**(5), 1030–1042

Emanuel, K. A. 1991 A scheme for representing cumulus convection in large-scale models. *J. Atmos. Sci.*, **48**, 2313–2335

1994 *Atmospheric convection*. Oxford University Press, New York, USA

1995 On thermally direct circulations in moist atmospheres. *J. Atmos. Sci.*, **52**, 1529–1534

Emanuel, K. A., Neelin, J. D. and Netherton, C. S. 1994 On large-scale circulations in convecting atmospheres. *Q. J. R. Meteorol. Soc.*, **120**, 1111–1143

Folland, C. K., Palmer, T. N. and Parker, D. E. 1986 Sahel rainfall and worldwide sea temperatures, 1901–85. *Nature*, **320**, 602–607

Glantz, M. H., Katz, R. W. and Nicholls, N. (Editors) 1991 *Telecommunications linking worldwide climate anomalies*. Cambridge University Press, Cambridge, United Kingdom

Gutman, G., Ohring, G. and Joseph, J. H. 1984 Interaction between the geobotanic state and climate: a suggested approach and a test with a zonal model. *J. Atmos. Sci.*, **41**, 2663–2678

Huffman, G. J., Adler, R. F., Rudoff, B., Schneider, U. and Keehn, P. R. 1995 Global precipitation estimates based on a technique for combining satellite-based estimates, rain gauge analysis and NWP model precipitation estimates. *J. Climate*, **8**(2), 1284–1295

Lamb, P. J. 1978a Case studies of tropical Atlantic surface circulation patterns during recent sub-Saharan weather anomalies: 1967 and 1958. *Mon. Weather Rev.*, **106**, 482–491

1978b Large-scale tropical Atlantic surface circulation patterns associated with sub-Saharan weather anomalies. *Tellus*, **30**, 240–251

Lamb, P. J. and Peppler, R. A. 1992 Further case studies of tropical Atlantic surface atmospheric and oceanic patterns associated with sub-Saharan drought. *J. Climate*, **5**(5), 476–488

Lough, J. M. 1986 Tropical sea surface temperature and rainfall variation in sub-Saharan Africa. *Mon. Weather Rev.*, **114**, 561–570

Manabe, S. 1969 Climate and the ocean circulation: I. The atmospheric circulation and the hydrology of the earth's surface. *Mon. Weather Rev.*, **97**, 739–774

Newell, R. E. and Kidson, J. W. 1984 African mean wind changes between Sahelian wet and dry periods. *J. Climatol.*, **4**, 27–33

Nicholson, S. E. and Palao, I. 1993 A re-evaluation of rainfall variability in the Sahel. Part I: Characteristics of rainfall fluctuations. *Int. J. Climatol.*, **13**, 371–389

Nicholson, S. E., Ba, M. B. and Kim, J. Y. 1996 Rainfall in the Sahel during 1994. *J. Climate*, **9**(7), 1673–1676

Owen, J. A. and Folland, C. K. 1988 Modelling the influence of sea surface temperatures on tropical rainfall. In *Recent climate change—a regional approach*. Ed. S. Gregory. Belhaven Press, London, UK

Owen, J. A. and Ward, M. N. 1989 Forecasting Sahel rainfall. *Weather*, **44**, 57–64

Parker, D. E., Folland, C. K. and Ward, M. N. 1988 Sea surface temperature anomaly patterns and prediction of seasonal rainfall in the Sahel region of Africa. In *Recent climate change—a regional approach*. Ed. S. Gregory. Belhaven Press, London, UK

Palmer, T. N. 1986 Influence of the Atlantic, Pacific and Indian Oceans on Sahel rainfall. *Nature*, **322**, 251–253

Palmer, T. N., Brankovic, C., Viterbo, P. and Miller, M. J. 1992 Modelling interannual variations of summer monsoons. *J. Climate*, **5**, 399–417

Plumb, R. A. and Hou, A. Y. 1992 The response of a zonally symmetric atmosphere to subtropical thermal forcing: threshold behavior. *J. Atmos. Sci.*, **49**, 1790–1799

Reynolds, R. and Smith, T. M. 1994 Improved global sea surface temperature analyses. *J. Climate*, **7**, 929–948

Rowell, D. P., Folland, C. K., Maskell, K., Owen, J. A. and Ward, M. N. 1992 Modelling the influence of global sea surface temperatures on the variability and and predictability of seasonal Sahel rainfall. *Geophys. Res. Lett.*, **19**, 905–908

Rowell, D. P., Folland, C. K., Maskell, K. and Ward, M. N. 1995 Variability of summer rainfall over tropical north Africa (1906–92): Observations and modelling. *Q. J. R. Meteorol. Soc.*, **121**, 669–704

Semazzi, F. H. M., Mehta, V. and Sud, Y. C. 1988 An investigation of the relationship between sub-Saharan rainfall and global sea surface temperatures. *Atmos.-Ocean*, **26**, 118–138

Srinivasan, J., Gadgil, S. and Webster, P. J. 1993 Meridional propagation of large-scale monsoon convective zones. *Meteorol. Atmos. Phys.*, **52**, 15–35

Sud, Y. C. and Lau, K. M. 1996 Comments on paper 'Variability of summer rainfall over tropical north Africa (1906–92): Observations and modelling' by Rowell *et al.* (1995). *Q. J. R. Meteorol. Soc.*, **122**, 1001–1006

Walker, J. and Rowntree, P. R. 1977 The effect of soil moisture on circulation and rainfall in a tropical model. *Q. J. R. Meteorol. Soc.*, **103**, 29–46

Xue, Y. and Shukla, J. 1993 The influence of land surface properties on Sahel climate. Part I: Desertification. *J. Climate*, **6**, 2232–2245

Zheng, X. and Eltahir, E. A. B. 1997 The response to deforestation and desertification in a model of West African monsoons. *Geophys. Res. Lett.*, **24**, 155–158

1998a The role of vegetation in the dynamics of West African monsoons. *Journal of Climate*, **11**(8), 2078–2096

1998b A soil moisture–rainfall feedback mechanism. 2: Numerical experiments. *Water Resources Research*, **34**(4), 777–786